Master of Science Thesis

Hyperspectral imaging for gas detection

Joakim Sjunnebo

Laser Physics, Department of Applied Physics,
School of Engineering Sciences
Royal Institute of Technology, SE-106 91 Stockholm, Sweden

Stockholm, Sweden 2015

Examensarbete inom ämnet tillämpad fysik för avläggande av civilingenjörsexamen inom utbildningsprogrammet teknisk fysik.

Graduation thesis on the subject applied physics for the degree of Master of Science in Engineering from the School of Engineering Physics.

TRITA-FYS-2015:39
ISSN 0280-316X
ISRN KTH/FYS/--15:39--SE

Abstract

A method to detect and identify gases from their electromagnetic absorption spectrum using hyperspectral imaging is investigated. Spectral information is multiplexed by an interferometer based on birefringent polarizing prisms, and the interferogram Fourier transformed to reconstruct the original spectrum. The method, which was originally designed for surveillance applications in the visible spectrum, is here adapted and optimized for optical gas imaging in the mid-wave infrared (3-5 µm), targeting the hydrocarbon gases as well as carbon dioxide and nitrous oxide. The complete hyperspectral image can be captured in a single exposure, eliminating the risk of scanning artifacts.

The method is analyzed and tested using simulations. Reconstructions of simulated gas spectra indicate that gases with moderately varying spectra can be detected and identified, whereas gases with more rapidly varying spectra can not.

Sammanfattning

En metod för att detektera och identifiera gas utifrån deras elektromagnetiska absorptionsspektrum genom hyperspektral avbildning undersöks. Spektral infomation multiplexas av en interferometer baserad på dubbelbrytande polariserande prismor, och interferogrammet Fouriertransformeras för att rekonstruera det ursprungliga spektrumet. Metoden, som ursprungligen skapades för tillämpningar inom övervakning och som var konstruerad för att operera med synligt ljus, anpassas och optimeras för optisk gasdetektering inom det infraröda mellanvågsområdet (3-5 µm), med inriktning mot kolvätegaser samt koldioxid och dikväveoxid. Kompletta hyperspektrala bilder kan erhållas inom en enda exponering, vilket eliminerar risken för skanningsartefakter.

Metoden analyseras och testas med simuleringar. Rekonstruktioner av simulerade gasspektra indikerar att gaser med måttligt varierande spektrum kan detekteras och identifieras, medan gaser med snabbt varierande spektrum inte kan det.

Acknowledgements

This thesis was suggested and sponsored by FLIR Systems AB in Sweden. I would like to thank my supervisor at FLIR, Jonas Sandsten, for the great support and encouragement that I have received during my work on this thesis. I would also like to thank my supervisor at KTH, Zhangwei Yu, for the academic supervision and guidance.

Contents

Chapter 1

Introduction

The list of adverse effects caused by gas leaks is long. Some gases are harmful to the environment and can contribute to global warming, hazardous gases can pose both short- and long-term risks, for example explosions and cancer, to both workers and the people living close to the leaking facility, and gas leaks cost the industry substantial amounts of money. Because many gases are invisible, they have to be detected by other means. Earlier instruments had to be in close contact with the gas, which made inspections time consuming, potentially dangerous for the inspector, and the risk of missing a leak was high. A newer method is based on infrared cameras which can detect and visualize gas. FLIR Systems in Sweden develops gas detection cameras which are able to produce a full picture of the depicted area with gas appearing as smoke on the camera's viewfinder or LCD. Two main types of cameras have been developed which operate in different wavelength bands: mid-wave infrared (3-5 µm) and long-wave infrared (7-14 µm). These cameras, which utilize a narrow-band spectral filter to single out the wavelength of interest, can *detect* and and *visualize* gases. However, because they only resolve a single wavelength, they are unable to *identify* gases, that is, determine which gases have been detected.

Cameras that can resolve a large number of wavelengths are called hyperspectral cameras. These instruments measure the spectrum of objects for each pixel in the image of a scene, and can be seen as a combination of a camera and a spectrometer. All atoms and molecules have a unique electromagnetic spectrum, a sort of spectral signature or fingerprint. Hence, the chemical composition of an object can be identified by measuring its spectrum. Hyperspectral imaging is used in a large number of applications, for example, in agriculture and environmental surveys to remotely identify the progress and health of growing crops and forests [1], in mining and oil industries to look for ore minerals and oil [2], in biotechnology and biomedical engineering to study cells and proteins with fluorescent microscopy [3], and in astronomy to obtain spatially-resolved spectral images [4]. Hyperspectral instruments can also be used for gas imaging, where gases can be detected and identified from their spectral signature. Several different instruments have been built specifically for this purpose, targeting different gases with absorption in different parts of the

electromagnetic spectrum. While all of these instruments have their advantages and disadvantages, it is not until recent years it has become possible for high sensitivity, ground-based, real-time, continuous monitoring of fugitive gas emissions [5, 6, 7].

The aim of this thesis is to identify a hyperspectral technology suitable for optical gas imaging, and to study the capabilities and limitations of the technology. This is done by studying the literature on existing hyperspectral methods, analyzing the chosen technology theoretically, and modelling and simulating the instrument.

The thesis is organized as follows. Chapter 2 introduces the basics of optical gas imaging and hyperspectral imaging. The chapter ends with a discussion on the feasibility of different types of hyperspectral technologies to optical gas imaging, and motivates the choice of the technology studied in-depth in the remainder of the thesis. Chapter 3 describes the technology in detail and provides the theoretical framework necessary to analyze it. Chapter 4 describes the design and optimization process to adapt the instrument, which was originally designed for surveillance and target identification in unmanned vehicles in the visible spectrum, to optical gas imaging in the infrared spectrum. This chapter also describes the two-dimensional computer model that was built to simulate and analyze the system. Chapter 5 describes the extension of the model to a full three-dimensional model of the system, which is used to simulate and reconstruct a couple of gas spectra. The last chapter, Chapter 6, summarizes the thesis and contains some concluding remarks.

Chapter 2

Background

This chapter gives a general introduction to the fundamental principles of gas imaging and spectral imaging. First, optical gas imaging with infrared cameras is described. This is followed by a description of hyperspectral imaging and why it is desirable to use hyperspectral techniques for gas imaging. The last section describes different types of hyperspectral technologies, together with their advantages and disadvantages to do optical gas imaging. Finally, the choice of the hyperspectral technology analyzed in-depth in the remainder of the thesis is motivated.

2.1 Optical gas imaging

Atoms absorb and emit radiation corresponding to electronic transitions between electron energy states. The energy of absorbed and emitted photons must equal the excitation and de-excitation energy of electrons to conserve energy. Because each transition has a specific energy difference, absorption and emission only occur for wavelengths corresponding to these specific energies. Perhaps the most well-known example of this is the absorption of solar radiation in the solar atmosphere, observed as dark lines, known as Fraunhofer lines, in the solar spectrum. Because the absorption and emission is unique to each element, the characteristic lines act as a kind of spectral signature or "spectroscopic fingerprint", a feature that can be used to identify elements. Most electronic transitions are in the ultraviolet or visible spectral range. However, many molecular gases have absorption and emission in the infrared spectral range. Molecules possess additional degrees of freedom compared to atoms, namely rotational and vibrational modes. As for the electronic transitions, rotational and vibrational excitations can only occur between specific energy states. Therefore, absorption and emission due to rovibrational transitions only occur for specific wavelengths. Thus, any atom or molecule can be identified by measuring its characteristic spectrum.

All techniques to detect gases by thermal imaging utilize absorption and emission of infrared radiation in rotational and vibrational bands of gas molecules. A schematic illustration of the working principle for absorption is shown in Fig. 2.1.

A background object of temperature T emits radiation with a certain spectrum. For example, if the emissivity of the surface of the object is 1, the object would emit as a black body, and the spectrum would follow Planck's law. The radiation passes through a gas plume of temperature $T_{\text{gas}} < T$. Some of the radiation, with wavelengths corresponding to the energy of rovibrational excitations, is absorbed by the gas. The radiation that reaches the detector of the camera thus lack certain wavelengths. This has the effect that the intensity at the detector is lower if there is some gas between the camera and the background object, than if there is no gas present at all. By placing a filter in front of the detector, the spectral region can be tuned to match an absorption band of a certain gas or a certain class of gases. A narrower filter yields a larger relative signal change, and thus a higher signal contrast and sensitivity. However, the total intensity decreases, so there is a trade-off that has to be tuned by analyzing the signal-to-noise ratio. If the gas is hotter than the background, the contribution from gas emission will be larger than absorption. Therefore, a hot gas between the camera and the background results in an increase in the signal. Apart from being absorbed and emitted, radiation can also be scattered, which happens when an excitation is immediately followed by de-excitation. In optical gas imaging applications, scattered radiation is often the result of hot objects other than the background, emitting radiation which is scattered by the gas and detected by the camera. Different measures to minimize its contribution is usually taken, e.g. shielding [8].

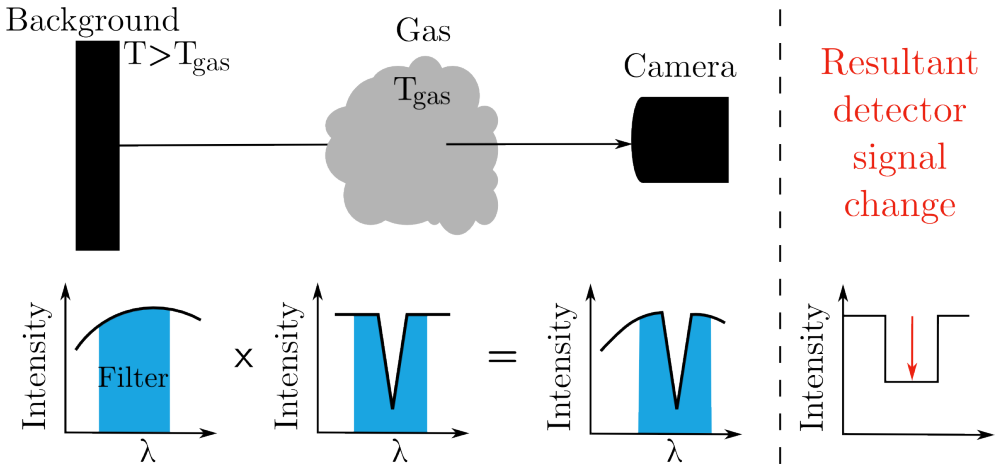

Figure 2.1: Illustration of the working principle of optical gas imaging by absorption. A hot background object emits radiation which passes through a cold gas. The gas absorbs some of the radiation, which results in a lower signal at the detector than in the absence of gas. Figure adapted from [8].

In addition to detecting gases, certain cameras can also perform a quantitative measurement of the gas concentration length, which is the concentration of the gas multiplied by the length of gas traversed by the radiation. Gas quantification requires knowledge about the temperature and emissivity (which in general is a

function of wavelength) of the background, the temperature of the gas, as well as detailed information about the transmission through the camera optics and the sensitivity of the detector. Furthermore, there is in general also absorption in the atmosphere by e.g. water vapour, that has to be accounted for.

Most gas cameras today utilize this single-filter technique in one way or another and can thus detect, and, in some cases, also quantify gas. However, there is no way to know which gas that has been detected with these cameras. To also identify a detected gas, the camera would have to measure the intensity of several wavelengths. These intensities would constitute a sampled spectrum, to be compared with known gas spectra and checked for a match.

2.2 Hyperspectral imaging

Conventional grayscale cameras produce images that describe the intensity $I(x, y)$ as a function of two spatial coordinates, x and y. Color cameras manage to reproduce the color of the scene by combining intensities from three separate color channels: red, green and blue. These channels correspond to three different bands in the visible spectrum. Hence, color cameras effectively produce images that describe the intensity $I(x, y, \lambda)$ as a function of the wavelength λ, in addition to the two spatial coordinates. Multispectral and hyperspectral cameras take this one step further by increasing the number of spectral bands. There is no clear distinction between multispectral and hyperspectral systems [9]. Generally, a system is considered multispectral if the number of spectral bands is less than ten, while systems with more spectral bands is considered hyperspectral. As this thesis mainly covers systems with more than ten spectral bands, the term hyperspectral will be used throughout the thesis.

The goal of hyperspectral imaging is to obtain a complete spectrum for each pixel of the image. Thus, each hyperspectral image consists of a three-dimensional dataset typically called a datacube. The three sides of the cube represent x, y and λ, and each element is the intensity $I(x, y, \lambda)$. The complication of hyperspectral imaging is that the datacubes are of a higher dimensionality than the currently available detectors, which are two-dimensional detector arrays. This can be solved by either collecting time-sequential 2D slices of the cube, or simultaneously measuring all elements of the cube by dividing it into multiple 2D elements, distributed and organized in some way on the detector array, and then recombining them into a cube during post-processing. These two techniques, which are depicted schematically in Fig. 2.2a and 2.2b, are referred to as *scanning* and *snapshot*, respectively. There are three main classes of scanning techniques. Spectral-scanning systems capture complete spatial images of the scene one spectral band at a time, for example by inserting a different filter in front of the detector for each image. Point-scanning systems capture a complete spectrum of each point of the scene, one point at a time. These systems typically disperse light from a single point of the scene onto a line-array detector, and were common before the advent of two-dimensional detector

arrays, when only line-array detectors were available. With the arrival of two-dimensional detector arrays, line-scanning systems became common. These systems image the scene one slice at a time, where light enters the system through a thin slit, and is dispersed onto the detector array.

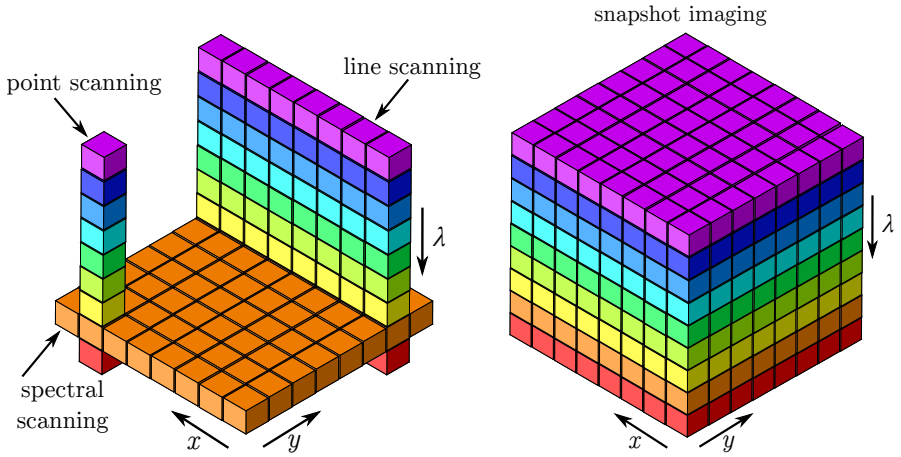

(a) Scanning **(b)** Snapshot

Figure 2.2: Illustration of the two different techniques to capture the datacube. Figure adapted from [9].

2.3 Selection of a hyperspectral technique for infrared gas imaging

A large number of different hyperspectral imaging techniques have been invented. The purpose of this section is not to summarize all of them, but rather to motivate the choice of technique made in this thesis. For an excellent review of the field and a summary of currently available techniques, see Ref. [9].

Each technique, of course, has different advantages and disadvantages, and is suited for different applications. In this thesis, the intended application is optical gas imaging, that is, detection, identification and possibly quantification of gas. This puts some requirements on the hyperspectral system, namely that the system is *fast* and *IR compatible*.

To continuously monitor potential gas leaks, the camera needs to be relatively fast. Fast here incorporates several aspects. First, the time required to capture a single hyperspectral image should be sufficiently short that the scene does not change significantly during this time. Scanning techniques, which require several exposures to capture the datacube, are generally slower than snapshot techniques [9]. If the scene is very dynamic, which can be the case for gas leaks, it changes between each exposure. Thus, each slice of the datacube would effectively sample slightly different scenes, which would lead to artifacts in the datacube. In the case of

spatial scanning, the position and extent of gas plumes (and other moving objects) would not be entirely accurate. Spectral scanning would lead to errors in the reconstructed spectrum for each pixel. Because of the risk of scanning artifacts in the datacube, scanning techniques were considered unsuitable for optical gas imaging, and only snapshot techniques were studied in more detail. Snapshot instruments have the further advantage of being more robust and often more compact than scanning instruments due to the lack of mechanically moving parts [10]. However, because the entire datacube has to be captured in a single integration period, the resolution is limited by the number of pixels in the detector array. The elements of the datacube have to fit on the detector array, whereby $N_x N_y N_\lambda \leq n \cdot m$, where N_x and N_y is the number of spatial elements in x and y, respectively, N_λ is the number of spectral elements, and n and m the number of pixels per row and column of the detector array. For scanning systems it is sufficient that the number of elements in each slice of the datacube is less than or equal to the number of pixels. Hence, the total number of elements, and thus the resolution, can be higher for scanning systems. To compensate for this, snapshot systems often utilize large detector arrays to maximize the number of pixels, and thus the potential resolution. To be able to monitor gas leaks in real-time, post-processing and reconstruction of the datacube must also be fast. Thus, computationally intensive techniques, such as Computed Tomography Imaging Spectrometry [11], which requires tomographic reconstruction, and Coded Aperture Snapshot Spectral Imaging [12], which is a compressive sensing technique that requires complex reconstruction of undersampled data, are unsuitable for optical gas imaging.

The system must be able to operate in the spectral range where the monitored gases have absorption peaks. There are several different ranges that are of interest. For example, many hydrocarbons have absorption in the lower mid-wavelength infrared (3-5 µm), and the potent greenhouse gas sulphur hexafluoride (SF_6) and several refrigerant gases have absorption in the long-wavelength infrared (7-14 µm). All components in the system must transmit (or reflect in the case of mirrors) radiation in the intended spectral range. Furthermore, systems with extremely small components, with sizes of the same order or less than the wavelength of the infrared light, are also unsuitable, because of unwanted diffraction effects which could reduce the performance. Most notably, this rules out systems that utilize digital micromirror arrays to direct the light.

To keep the complexity and cost of the system low, techniques utilizing more than one detector, e.g. [13, 14], were not considered.

The remaining systems utilize either spectral filters, prisms, diffraction gratings or interferometers to extract the spectral information. Techniques utilizing interferometers, also called Fourier transform infrared spectroscopy, have two major advantages compared to filtering and dispersive techniques. These advantages are called Fellgett's advantage and Jacquinot's advantage.

Fellgett's advantage, also called the multiplex advantage, is an improved signal-to-noise ratio of interferometric measurements compared to direct measurements [15]. This stems from the fact that with filters and dispersive elements, such as

prisms and gratings, only one wavelength is measured at a time. That is, each pixel receives only a fraction of the total intensity of the light, since only a single wavelength reaches each pixel (all other wavelengths have been filtered out or dispersed to other pixels). Interferometers, on the other hand, multiplex the signal, which means that the spectral information from all wavelengths are measured simultaneously. Thus, the intensity of the signal is not reduced by filtering or dispersing the signal, which results in a higher signal-to-noise ratio for interferometer-based systems.

Jacquinot's advantage, or the throughput advantage, is an improved signal-to-noise ratio due to the higher optical throughput of interferometers compared to dispersive elements, which require small entrance slits that restrict the amount of light that passes through them [16].

A high signal-to-noise ratio is very important in optical gas imaging systems, particularly for quantitative measurements. Systems utilizing interferometers are therefore well suited for gas imaging. Multiple-Image Fourier Transform Spectral Imaging [17] is a technique combining a two-dimensional lenslet array with a Michelson interferometer. Although the mirror interferometer makes it well suited for infrared optical gas imaging, the alignment of the mirrors is very sensitive. Thus, vibrations, thermal expansion, air turbulence and other effects can affect the measurements. A more robust instrument, which is less sensitive to vibrations, is the Snapshot Hyperspectral Imaging Fourier Transform Spectrometer [18, 19]. It replaces the Michelson interferometer in the former instrument by a birefringent polarization interferometer, made of birefringent prisms. This technique was, due to the discussion above, considered promising for optical gas imaging applications, and is the topic for the remainder of the thesis.

Chapter 3

Theory

This chapter introduces the theoretical concepts of the hyperspectral technology chosen in Chapter 2, the Snapshot Hyperspectral Imaging Fourier Transform Spectrometer. First, the concept of birefringence and ray tracing through uniaxial media is discussed. This is followed by a description of the working principles of the birefringent polarization interferometer and the hyperspectral imaging system. Finally, interference is discussed in relation to how the hyperspectral images are formed on the detector.

3.1 Birefringence

Not all materials are optically isotropic. Birefringent materials have a refractive index that depends on both the polarization and the propagation direction of light. The most common type of birefringent media has one symmetry axis and is called uniaxial. This axis, called the optic axis, governs the anisotropy and defines a special direction of the media. All directions at a given angle to the optic axis is optically equivalent. Uniaxial media split an incident beam into two rays: one, called the ordinary ray (o-ray), with the polarization perpendicular to the optic axis, and the other, called the extraordinary ray (e-ray), with the polarization partly in the direction of (but not necessarily parallel to) the optic axis [20].

Formulas for ray tracing of the o-ray and e-ray through uniaxial media has been derived in e.g. [20, 21, 22, 23]. The following treatment largely follows [21], but slightly generalizes some results.

The ordinary wave (o-wave) obeys Snell's law,

$$n_1 \sin\theta_1 = n_\mathrm{o} \sin\theta_\mathrm{o}, \tag{3.1}$$

where n_1 is the refractive index of the incident medium, θ_1 is the incident angle, n_o is the refractive index of the o-wave in the birefringent material, and θ_o the o-wave angle of refraction. The extraordinary wave (e-wave) obeys a similar law,

$$n_1 \sin\theta_1 = n \sin\theta_\mathrm{e}, \tag{3.2}$$

where θ_e is the angle of refraction for the e-wave, and n is the effective refractive index for the e-wave. The difference between the two formulas is that n_o is a constant, whereas n is a function of the angle between the e-wave vector and the optic axis. Denoting this angle by θ, we have

$$n = \frac{n_\mathrm{o} n_\mathrm{e}}{\sqrt{n_\mathrm{o}^2 \sin^2\theta + n_\mathrm{e}^2 \cos^2\theta}}, \tag{3.3}$$

where n_e is the extraordinary refractive index. Note that n varies between the two extreme values n_o and n_e for different θ. n_o and n_e are both properties of the birefringent medium, and is usually expressed as the birefringence $B = n_\mathrm{e} - n_\mathrm{o}$.

In isotropic media, the wave vector $\mathbf{k}$ and the ray vector (Poynting vector) $\mathbf{S}$ point in the same direction. However, in birefringent media, this is only true for the ordinary ray. For the extraordinary ray, the wave vector $\mathbf{k}_\mathrm{e}$ and the ray vector $\mathbf{S}_\mathrm{e}$ are not parallel, which means that the power flow, given by the Poynting vector, is not in the same direction as the surfaces of constant phase. Because the ordinary wave vector and ray vector are the same, Eq. 3.1 fully describes the ordinary refraction.

To calculate the extraordinary wave vector and ray vector, we consider the arrangement in Fig. 3.1. A monochromatic plane wave $\hat{\mathbf{k}}_1$ falls on the plane surface of a birefringent medium. The coordinate system is chosen so that the x-axis is parallel to the surface normal $\hat{\mathbf{n}}$, and the yz-plane is coincident with the surface. $\hat{\mathbf{k}}_\mathrm{e}$ is the refracted e-wave vector, $\hat{\mathbf{S}}_\mathrm{e}$ is the refracted e-ray vector, and $\hat{\mathbf{w}}$ is the optic axis. The phase matching condition [24],

$$\hat{\mathbf{k}}_1 \cdot \mathbf{r} = \hat{\mathbf{k}}_\mathrm{e} \cdot \mathbf{r}, \tag{3.4}$$

where $\mathbf{r}$ is any point on the surface, imply that the e-wave vector $\hat{\mathbf{k}}_\mathrm{e}$ is in the plane of incidence (the xy-plane). Hence, $\hat{\mathbf{k}}_\mathrm{e} = (\cos\theta_\mathrm{e}, \sin\theta_\mathrm{e}, 0)$, where θ_e is the angle of refraction for the e-wave. Let $\hat{\mathbf{w}} = (x_0, y_0, z_0)$, then, because the angle between the optic axis and the e-wave vector is θ,

$$\hat{\mathbf{k}}_\mathrm{e} \cdot \hat{\mathbf{w}} = \cos\theta = x_0 \cos\theta_\mathrm{e} + y_0 \sin\theta_\mathrm{e}. \tag{3.5}$$

Substituting this into Eq. 3.3, we get

$$n = \frac{n_\mathrm{o} n_\mathrm{e}}{\sqrt{n_\mathrm{o}^2[1 - (x_0\cos\theta_\mathrm{e} + y_0\sin\theta_\mathrm{e})^2] + n_\mathrm{e}^2(x_0\cos\theta_\mathrm{e} + y_0\sin\theta_\mathrm{e})^2}}. \tag{3.6}$$

Inserting this into Eq. 3.2 and simplifying, we get a quadratic equation in $\cot\theta_\mathrm{e}$,

$$\begin{aligned}[n_\mathrm{o}^2 + x_0^2(n_\mathrm{e}^2 - n_\mathrm{o}^2)]\cot^2\theta_\mathrm{e} + 2x_0y_0(n_\mathrm{e}^2 - n_\mathrm{o}^2)\cot\theta_\mathrm{e} \\ + n_\mathrm{o}^2 + y_0^2(n_\mathrm{e}^2 - n_\mathrm{o}^2) - \frac{n_\mathrm{o}^2 n_\mathrm{e}^2}{n_1^2 \sin^2\theta_1} = 0.\end{aligned} \tag{3.7}$$

Solving this equation, we get

$$\cot\theta_\mathrm{e} = \frac{-2x_0y_0(n_\mathrm{e}^2 - n_\mathrm{o}^2) \pm 2n_\mathrm{o}\sqrt{\frac{n_\mathrm{o}^2 n_\mathrm{e}^2 + n_\mathrm{e}^2 x_0^2 (n_\mathrm{e}^2 - n_\mathrm{o}^2)}{n_1^2 \sin^2\theta_1} - [n_\mathrm{o}^2 - (n_\mathrm{e}^2 - n_\mathrm{o}^2)(x_0^2 + y_0^2)]}}{2[n_\mathrm{o}^2 + x_0^2(n_\mathrm{e}^2 - n_\mathrm{o}^2)]}. \tag{3.8}$$

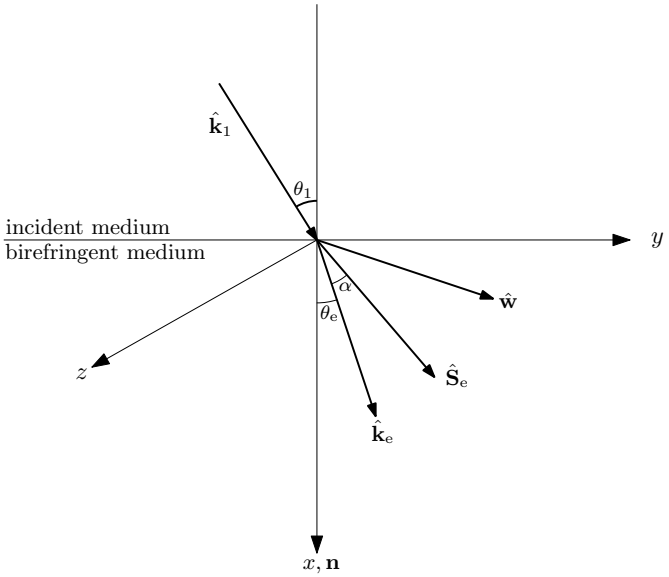

Figure 3.1: Illustration of extraordinary ray and wave vector refraction in uniaxial media. A wave vector $\hat{\mathbf{k}}_1$ is incident on the surface of a birefringent medium at an angle θ_1. The extraordinary wave vector $\hat{\mathbf{k}}_e$ is refracted with an angle θ_e and the extraordinary ray vector $\hat{\mathbf{S}}_e$ is an angle α from $\hat{\mathbf{k}}_e$. The optic axis is denoted by $\hat{\mathbf{w}}$ and the coordinate system is chosen so that the x-axis is the surface normal $\mathbf{n}$. Figure adapted from [21].

Only one of the solutions will be physically reasonable, corresponding to the solution that lies between the two extreme values of θ_e when n_o and n_e is substituted into Eq. 3.2.

It can be shown that the angle between $\hat{\mathbf{k}}_e$ and $\hat{\mathbf{S}}_e$ is given by [21]

$$\alpha = \frac{(n_e^2 - n_o^2)\tan\theta}{n_e^2 + n_o^2 \tan^2\theta}. \tag{3.9}$$

α can also be related to $\hat{\mathbf{k}}_e$ and $\hat{\mathbf{S}}_e$ through their scalar product,

$$\hat{\mathbf{S}}_e \cdot \hat{\mathbf{k}}_e = \cos\alpha. \tag{3.10}$$

In general, $\hat{\mathbf{S}}_e$ is not in the incident plane. However, it is coplanar with $\hat{\mathbf{w}}$ and $\hat{\mathbf{k}}_e$,

$$\hat{\mathbf{S}}_e \cdot \hat{\mathbf{w}} \times \hat{\mathbf{k}}_e = 0. \tag{3.11}$$

Combining Eq. 3.5, 3.9, 3.10 and 3.11, together with the normalization condition on $\hat{\mathbf{S}}_e = (S_x, S_y, S_z)$, yields

$$S_x = \cos\alpha\cos\theta_e + \frac{\sin\theta_e \sin\alpha(x_0\sin\theta_e - y_0\cos\theta_e)}{\sqrt{z_0^2 + (x_0\sin\theta_e - y_0\cos\theta_e)^2}}, \tag{3.12}$$

$$S_y = \cos\alpha\sin\theta_e - \frac{\cos\theta_e \sin\alpha(x_0\sin\theta_e - y_0\cos\theta_e)}{\sqrt{z_0^2 + (x_0\sin\theta_e - y_0\cos\theta_e)^2}}, \tag{3.13}$$

$$S_z = \frac{z_0\sin\alpha}{\sqrt{z_0^2 + (x_0\sin\theta_e - y_0\cos\theta_e)^2}}. \tag{3.14}$$

With these equations, the propagation of both the ordinary and the extraordinary rays and waves can be calculated in any uniaxial medium.

The final result from this treatment, which we will be needed later in the thesis when calculating optical path lengths, is the effective refractive index for the e-ray vector n_{S}, which is

$$n_{\mathrm{S}} = n \cos \alpha. \tag{3.15}$$

3.2 Birefringent polarization interferometer

The central component of the hyperspectral camera studied in this thesis is the birefringent polarization interferometer (BPI), depicted schematically in Fig. 3.2. Unpolarized light incident from the left is polarized by a linear generating polarizer (G). The polarizer, which is oriented at 45° in the xy-plane, generates a polarization state that is a superposition of equal parts x and y polarization. A Nomarski prism (NP) [25, 26], consisting of two uniaxial birefringent crystals wedged together with a wedge angle γ, splits the linearly polarized beam into two orthogonally polarized beams. These beams are the ordinary and the extraordinary rays of the uniaxial crystal. The optic axis of the first wedge is oriented at an angle δ in the zx-plane. As stated in Sec. 3.1, the ordinary ray always has a polarization perpendicular to the optic axis, so its polarization is in the y-direction. The extraordinary ray, which always has a polarization component in the direction of the optic axis, is polarized in the x-direction. In the figure, the path of the two polarization states x and y is represented by the red dashed and the blue solid lines, respectively. In the second crystal wedge, the optic axis is parallel to the y-axis. Thus, the ray that was ordinary in the first wedge becomes extraordinary in the second wedge, since the polarization of the ray is unchanged by the refraction and still is in the y-direction, i.e. parallel to the optic axis of the second wedge. Similarly, the extraordinary ray in the first wedge becomes ordinary in the second. After the first Nomarski prism, a half-wave plate (HWP), oriented at 45° in the xy-plane, rotates the polarization states 90° so that the polarization direction of the two orthogonally polarized rays are switched. Hence, the ray that was x polarized before the HWP becomes y polarized, and vice versa. A second Nomarski prism (NP2), identical to NP1 but rotated 180°, focuses the two rays so that they intersect in a plane parallel to the xy-plane. Since the rays travel different paths through the prisms, there will be an optical path difference Δ between them. Δ depends on the distance from the point where the ray strikes the BPI to the BPI symmetry plane that is coplanar with the yz-plane (where the wedges have the same thickness). Hence, Δ depends on the x-position and, in general, the angle of the incident ray, and determines the interference fringe pattern, which will be discussed in Sec. 3.3. The fringes are localized in the plane where the rays intersect, the fringe localization plane (FL). A second polarizer (A), identical to G, analyzes the rays into a coherent polarization state, enabling interference fringes to be formed on a detector.

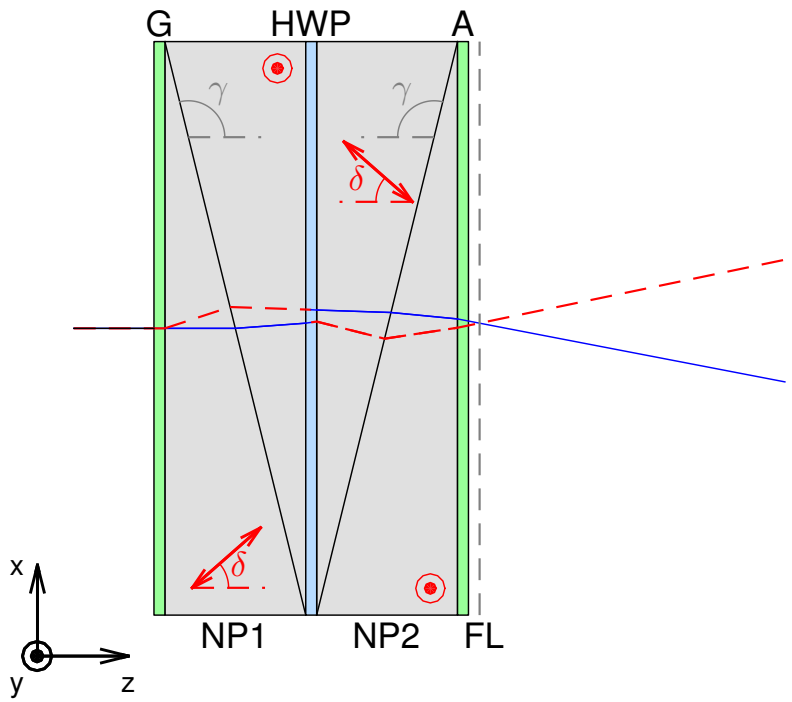

Figure 3.2: The birefringent polarization interferometer (BPI), consisting of a generating polarizer (G), two Nomarski prisms (NP1) and (NP2), a half-wave plate (HWP) and an analyzer (A). The interference fringes are localized in the fringe localization plane (FL). The red dashed and blue solid lines represent the path of the x and y polarized rays, respectively. The separation of the rays is exaggerated for illustrative purposes.

Figure 3.3 shows the birefringent polarization interferometer incorporated into the snapshot hyperspectral imaging system. An object is imaged by a two-dimensional array of smaller lenses, a lenslet array, which creates an array of identical sub-images of the object. The images are transmitted through the birefringent polarization interferometer, which creates an optical path difference as a function of the x-position and angle of the incident ray. The distance between the lenslet array and the BPI, and the focal length of the lenslets, are chosen so that the focal planes of the lenslets are coincident with the fringe localization plane. This makes the sub-images coincident with the interference fringes. By placing the focal plane array (FPA) at this position, an array of focused sub-images together with an interference pattern is recorded on the detector. The BPI is rotated an angle ψ around the z-axis with respect to the lenslet array and FPA, which introduces a y-position dependence in Δ. This follows from the fact that the BPI symmetry plane is rotated, so the distance to this plane will depend on y for a given x.

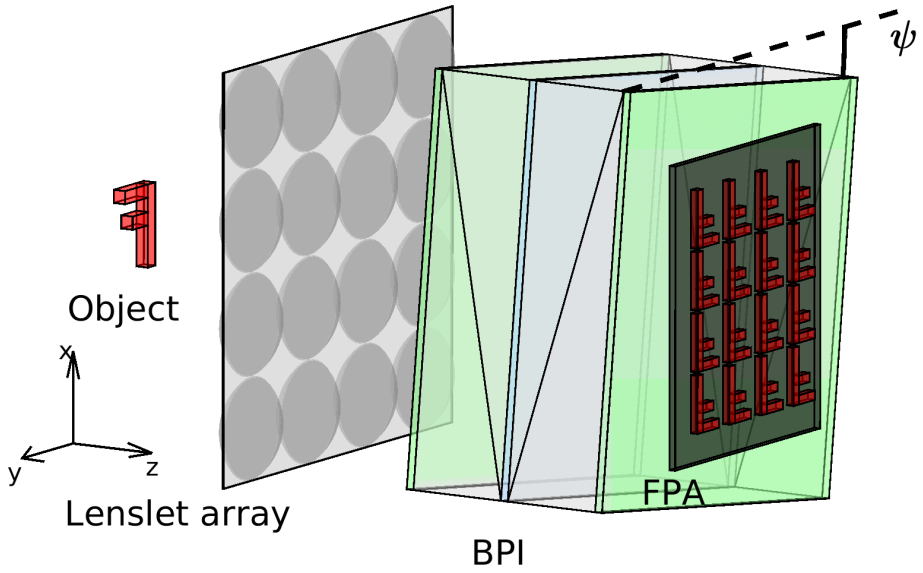

Figure 3.3: Schematic figure of the snapshot hyperspectral imaging interferometer. A lenslet array creates an array of identical sub-images of the object. These sub-images are transmitted through the BPI, which is rotated an angle ψ around the z-axis, and focused in the FL plane, where the FPA is located.

3.3 Interference

The interference of two monochromatic beams of the same wavenumber $\tilde{\nu} = 1/\lambda$ is given by [24]

$$I = I_1 + I_2 + 2\sqrt{I_1 I_2}\cos(\phi_2 - \phi_1), \tag{3.16}$$

where I_1 and I_2 are the intensities of the beams, ϕ_1 and ϕ_2 the phase of the beams, and I the total resultant intensity. The phase of a beam is $\phi = 2\pi\tilde{\nu}L$, where L is the optical path length of the beam, i.e. the distance travelled multiplied by the refractive index. The difference in optical path lengths of two beams is $L_2 - L_1 = \Delta$, which is the optical path difference. Substituting this in Eq. 3.16 and setting $I_1 = I_2 = \frac{1}{2}I_0$, where I_0 is some source intensity, yields

$$I(\Delta) = I_0(1 + \cos(2\pi\tilde{\nu}\Delta)). \tag{3.17}$$

For a source emitting a spectrum of wavenumbers $I(\tilde{\nu})$, the intensity as a function of Δ can be expressed as [16]

$$I(\Delta) = \int_0^\infty I(\tilde{\nu})(1 + \cos(2\pi\tilde{\nu}\Delta))\mathrm{d}\tilde{\nu}. \tag{3.18}$$

This can be rewritten as [27]

$$I(\Delta) = \frac{1}{2}\int_{-\infty}^{\infty} I(\tilde{\nu})(1 + \mathrm{e}^{i2\pi\tilde{\nu}\Delta})\mathrm{d}\tilde{\nu}. \tag{3.19}$$

The spectrum of the source $I(\tilde{\nu})$ is recovered by Fourier transforming the interferogram $I(\Delta)$,

$$I(\tilde{\nu}) = \mathfrak{F}[I(\Delta)] = \frac{1}{2}\int_{-\infty}^{\infty} I(\Delta)(1 + \mathrm{e}^{-i2\pi\tilde{\nu}\Delta})\mathrm{d}\Delta. \tag{3.20}$$

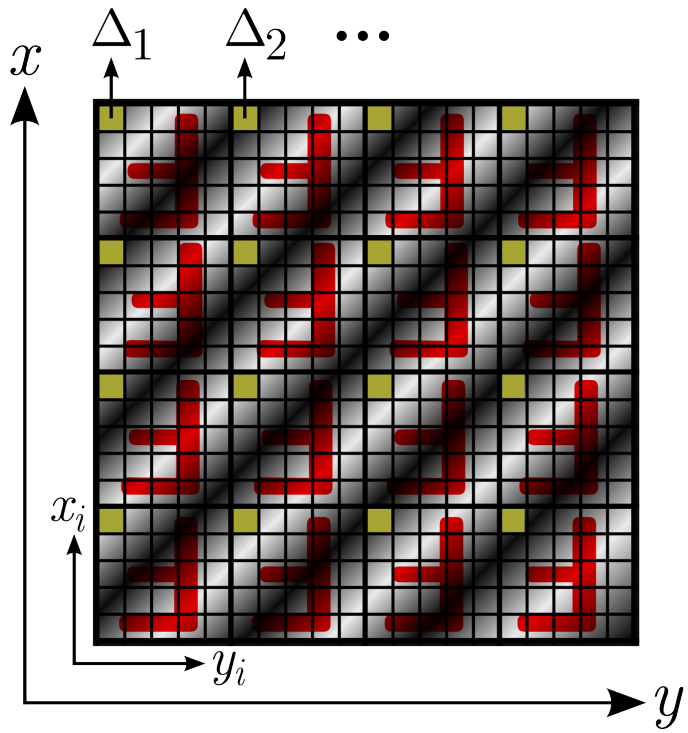

Figure 3.4: Schematic figure depicting the arrangement of sub-images on the FPA. The global coordinate system xy is the same as in Fig. 3.3, whereas the $x_i y_i$ system is local to sub-image i, for $i \in \{1, 2, ..., N \times M\}$, and describes the relative position within a sub-image. Each pixel at the same relative position within the sub-images experience a different Δ and therefore detect a different intensity. The intensities of all these pixels make up the interferogram for the corresponding point on the object.

Let the number of lenslets in the lenslet array be $N \times M$. Then there will be $N \times M$ sub-images on the FPA, see Fig 3.4. As stated in Sec. 3.1, the rotated BPI creates an optical path difference Δ that is a function of x, y, and, in general, the incident angle θ_1. The influence of θ_1 is small compared to x and y and can for the sake of this argument be ignored. First consider the case $\psi = 0$. Then $\Delta = \Delta(x)$ and all optical path differences will be the same within each row of pixels. Hence, the intensities of each pixel at the same relative position within the sub-images on the same row will be the same. If $\psi \neq 0$, on the other hand, $\Delta = \Delta(x, y)$ and all

pixels will sample a different optical path difference. The result is $N \times M$ focused sub-images on the FPA, modulated by an interference fringe pattern determined by the spectral properties of the scene. In Fig. 3.4, the fringe pattern is depicted by the light and dark stripes.

The intensities of all pixels at the same relative position within the sub-images form an interferogram of the corresponding point on the object. In Fig 3.4, for example, the intensities of the pixels marked yellow make up the interferogram for the lower-right (since the image is reflected horizontally and vertically) point on the object. The spectrum of the point is reconstructed by taking the Fourier transform of the interferogram using Eq. 3.20. The full hyperspectral image is constructed by repeating this procedure for all pixels in the sub-image.

Chapter 4

Design and Optimization

This chapter describes the methods that were used to design and optimize the hyperspectral imaging system. First, the simulation model of the birefringent polarization interferometer that was built is described in detail. This is followed by a description of how the BPI was designed and optimized using the simulation model. The chapter ends with a description of the optical design, together with simulations of the full hyperspectral imaging system.

4.1 Interferometer model

A 2D model of the birefringent polarization interferometer was built in MATLAB. Figure 4.1 shows an example of a simulation of a ray through the model.

A flowchart visualizing the steps involved in the simulation is shown in Fig. 4.2. The first step was to set up the following system parameters for the simulation:

- thickness, height and position of polarizers, prisms and half-wave plate,
- refractive index of polarizers, prisms, half-wave plate and surrounding medium,
- ordinary and extraordinary refractive indices of prisms,
- wedge angle γ and optic axis inclination angle δ, and,
- whether to run the simulation with or without a half-wave plate.

The next step was to set the incident angle and x-position of the incoming ray. The incident angle, refractive indices, wedge angle and optic axis inclination angle were used to calculate the angle of refraction for the ordinary ray and the extraordinary ray vector and wave vector as described in Sec. 3.1. The effective refractive indices n and n_{S} were also calculated. The calculations were repeated for each interface of the first prism, where the angles of refraction from the preceding interface were used as incident angles for the following interface. The extraordinary wave vector, as opposed to ray vector, were used to calculate the extraordinary incident angle at each interface [20]. After the angles and refractive indices had been calculated

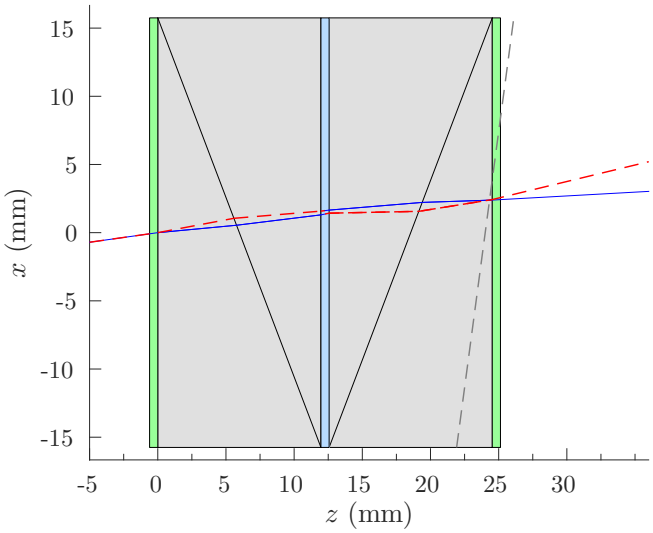

Figure 4.1: Simulation of a ray through the BPI model implemented in MATLAB. Green areas represent polarizers, gray areas birefringent prisms, and the blue area represent the half-wave plate. Red dashed lines represent y polarization and blue solid lines x polarization. The gray dashed line indicate the fringe localization plane.

for the first prism, the path of each ray was traced from the first interface of the first prism to the first interface of the second prism. This was done by tracing the ray vectors between each interface. The half-wave plate was modelled as an ideal half-wave plate that rotated the polarization states exactly 90°. The effect of the polarization rotation was only implemented if the simulation was set up to include the half-wave plate. Next, the calculations performed on the first prism were repeated for the second prism. The incident angles and starting positions were taken from the ray tracing in the first prism. The difference for the second prism was that the rays were already polarized in the x- and y-direction, and therefore would not split into two in the second prism. After the rays had been traced in the second prism, the position and inclination of the fringe localization plane was calculated by finding two points on the plane (which in the this 2D model was a straight line) [20]. The first point was the intersection of the two orthogonally polarized rays exiting the second prism. If the rays were divergent, they were extrapolated back and their intersection point found inside the prism. The second point on the line was found by repeating the ray tracing for a ray with the same incident angle but another x-position, and finding the intersection point of the two new rays exiting the second prism. After the fringe localization plane had been determined, the optical path length of a ray was calculated as

$$\begin{aligned} L = &\sum_{i=1}^{4} n_i \sqrt{(z_{i+1} - z_i)^2 + (x_{i+1} - x_i)^2} \\ &+ \operatorname{sgn}(z_{\mathrm{FL}} - z_5) n_5 \sqrt{(z_{\mathrm{FL}} - z_5)^2 + (x_{\mathrm{FL}} - x_5)^2}, \end{aligned} \tag{4.1}$$

where (x_i, z_i) was the intersection point with interface i, starting from the first prism's surface, n_i the refractive index for the ray in the region between interface i and $i+1$, and $(z_{\mathrm{FL}}, x_{\mathrm{FL}})$ the intersection point with the fringe localization plane. The last term, which was the contribution from the ray segment between the second prism's last surface and the fringe localization plane, could take on two different values. If the rays exiting the second prism were convergent, that is, if $z_{\mathrm{FL}} > z_5$, the term was added. However, if the rays were divergent, that is, if $z_{\mathrm{FL}} < z_5$, the fringes were virtual and localized within the prism. In this case, the optical path length was corrected by subtracting the last term instead of adding it, which was the task of the sgn-function. In the regions where the ray was extraordinary, the effective refractive index was n_S. Finally, the optical path difference Δ was calculated as $\Delta = L_y - L_x$, where the subindices refer to the polarization of the rays at the fringe localization plane [20].

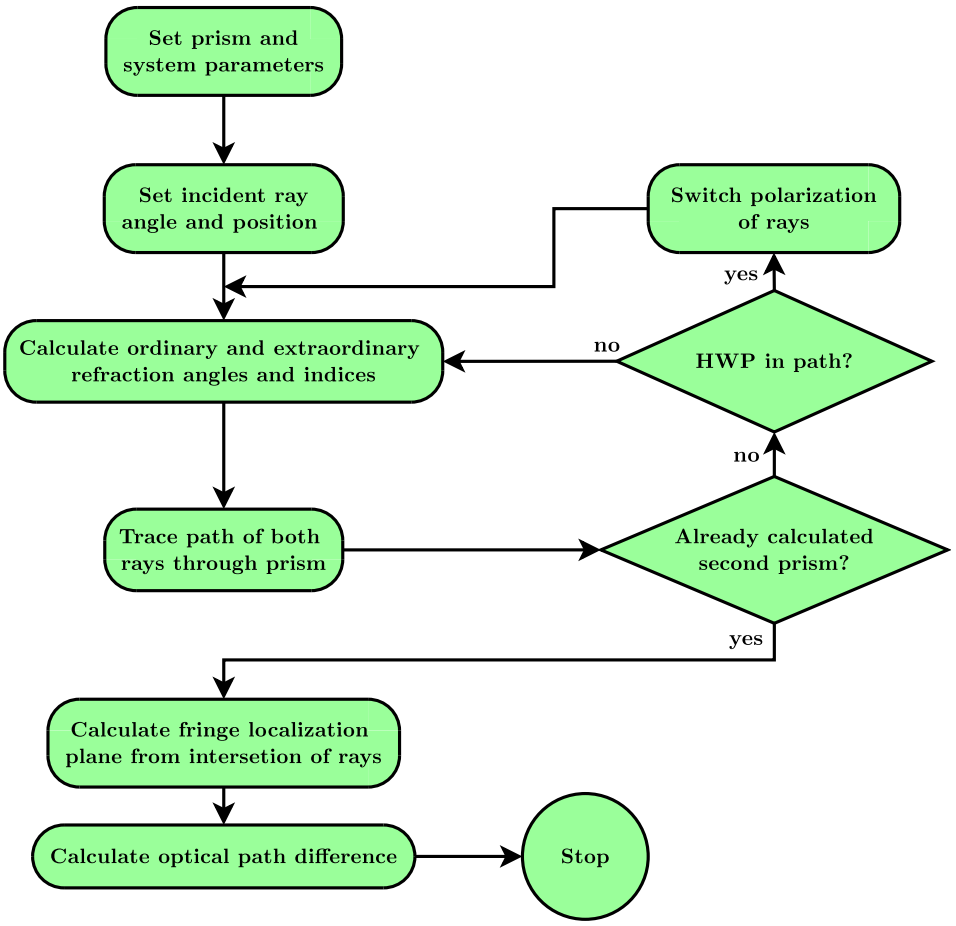

Figure 4.2: Flowchart of the birefringent polarization interferometer ray trace and optical path difference calculation algorithm.

4.2 Interferometer design and optimization

An important part of the development process was to determine the specifications for the BPI. This involved deciding what the values of the parameters listed in the beginning of Sec. 4.1 should be in order to adapt the BPI, which was originally designed to operate in the visible spectrum [18, 19], to operate optimally in the infrared spectrum. Furthermore, the intended application to gas imaging also had an impact on the design considerations.

Prism material

The Nomarski prisms had to be made of a material that fulfil two requirements: it should be birefringent and have acceptable transmission in the infrared. Two of the few materials that fulfil these requirements are rutile (TiO_2) and sapphire (Al_2O_3). Rutile has a birefringence of $B = +0.17$ at 3.38 µm and a transmission range of 0.4–5 µm [28, 29]. Sapphire has a relatively low birefringence of $B = -0.008$ at 3.33 µm and a transmission range of 0.5–5.5 µm [30]. Both transmission ranges cover the mid-wave infrared region, where many hydrocarbons have absorption, as well as carbon dioxide and nitrous oxide, making both materials suitable for optical gas imaging of these gases. A limiting factor of rutile is that its mechanical and physical properties make it difficult to manufacture thin crystal wedges of it [31], which limits its possible applications. With sapphire, however, it is possible to manufacture both thinner and thicker crystal wedges, and also specify the optic axis orientation to sub-degree precision [30]. Therefore, sapphire was chosen as the prism material to base the design on.

Polarizers and half-wave plate

The dimensions and materials of the polarizers and the half-wave plate were taken from off-the-shelf products available from major manufacturers and distributors (e.g. [32, 33]). The wave plate was therefore assumed to be 0.6 mm thick and made of cadmium thiogallate, and the polarizers to be of wire grid type on 2 mm thick silicon substrate. Both cadmium thiogallate and silicon transmit in the 3-5 µm region.

Lenslets and detector

The number of lenslets in the lenslet array determines the spatial resolution of the hyperspectral images. Let the number of pixels on the FPA be $n \times m$, where n and m is the number of pixels per row and column, respectively. Then the sub-images, and hence the reconstructed hyperspectral image, will have a spatial resolution of $n/N \times m/M$ pixels, where N and M is the number of lenslets per row and column, respectively. The number of lenslets also determine the spectral resolution, as the number of spectral sample points in the reconstructed spectrum is proportional to the number of sub-images [16]. Hence, there is a trade-off between spectral and

spatial resolution; the former increases with the number of lenslets, whereas the latter decreases. To utilize as many of the pixels on the FPA as possible, the number of sub-images and their aspect ratio should be matched to FPA format. This can be achieved by choosing N and M so that the remainder of n/N and m/M is zero. The aspect ratio of the sub-images is $n/N : m/M$. If $N = M$, the sub-images will have the same aspect ratio as the FPA, and the number of lenslets per row and column will be equal. If $N \neq M$, the aspect ratio of the sub-images will in general not be the same as that of the FPA, but can often be chosen to be $1:1$ (square format), which has the advantage of an x–y symmetry in the incident angles on the BPI from each lenslet. In this case, the magnitude of the effect of incident angle on optical path difference will be the same in both directions for each sub-image.

To maximize the sensitivity, the FPA was assumed to be of a high quantum efficiency cooled type, in favor of uncooled technologies such as microbolometer detectors. In order to get high resolution hyperspectral images, the FPA was further assumed to be of a large format. A common large format for cooled detectors, $n \times m = 1280 \times 1024$ pixels with a pitch of 15 µm, was used in the subsequent design and analysis. The number of lenslets was chosen to be $N \times M = 10 \times 8$, matching the FPA aspect ratio of $5:4$ and yielding square format images. Spatial resolution was sacrificed in favour of spectral resolution by choosing 10×8 lenslets rather than 5×4. This was motivated by the fact that gas plumes inherently are quite "diffuse", whereby the spatial resolution needed to resolve them is relatively low, and that a high spectral resolution is needed to identify gas spectra. With 10×8 sub-images, the spatial resolution becomes 128×128 pixels.

Spectral resolution

To properly reconstruct the spectrum without aliasing, the sampling frequency needs to be at least twice the frequency of the signal. For a broadband signal, the highest frequency component determines the Nyquist frequency. Put another way, the shortest wavelength that can be reconstructed $\lambda_{\min}$ is equal to twice the difference in optical path differences between two consecutive interferogram points. Thus,

$$\frac{\lambda_{\min}}{2} = \Delta_{\text{Nyquist}} = \Delta(x_{i+1}, y_{i+1}) - \Delta(x_i, y_i), \tag{4.2}$$

where Δ_{Nyquist} is the critical sampling optical path difference. Because the intensity (see Eq. 3.18) is independent of the sign of Δ, only one side of the interferogram is unique and contributes to the resolution of the reconstructed spectrum. The spectral resolution, i.e. the smallest resolvable difference in wavenumber, is $\Delta\tilde{\nu} = 1/\Delta_{\max}$, where $\Delta_{\max}$ is the largest optical path difference in the interferogram [16]. Here $\Delta_{\max} = n_+\Delta_{\text{s}}$, where n_+ is the number of positive interferogram points, or, equivalently, the number of lenslets that sample positive optical path differences, and Δ_{s} is some sampling period. Figure 4.3 shows an example of an interferogram illustrating

Δ_s, n_+ and Δ_{max}. Minimizing $\Delta\tilde{\nu}$ (smaller $\Delta\tilde{\nu}$ means better resolution) is equivalent to maximizing Δ_{max}. To be able to reconstruct a chosen λ_{min}, the sampling period is constrained by the Nyquist criterion, $\Delta_s \leq \Delta_{Nyquist} = \lambda_{min}/2$. The equality $\Delta_s = \Delta_{Nyquist}$ maximizes Δ_{max}. n_+ is maximized when a purely single-sided interferogram is collected, i.e. when only positive Δ is sampled. Purely single-sided interferograms are, however, extremely sensitive to a type of error called phase errors. These errors, which can arise from misplacement of the zero optical path difference point, lead to errors in the reconstructed spectrum [27]. Double-sided interferograms, which contain an equal number of positive and negative interferogram points, are very stable in regard to phase errors, and the output spectra essentially unaffected. Because purely single-sided interferograms are so sensitive to phase errors, the maximum attainable spectral resolution is usually sacrificed for an increased stability against phase errors. This is achieved through a technique called phase correction, which entails sampling a few negative Δ and a majority of positive Δ. The negative samples are used to correct the phase of the spectrum that results from the larger, positive part of the interferogram [27]. A commonly used rule of thumb is that 25 % negative interferogram points provide enough stability against phase errors [16].

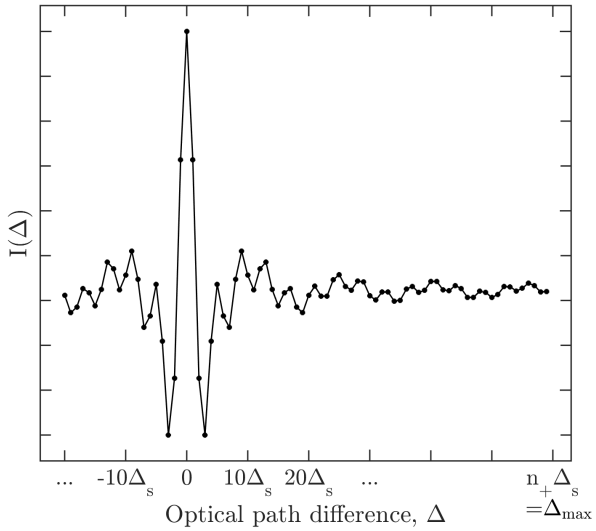

Figure 4.3: Schematic figure of a one-sided interferogram. The distance between each point is the sampling optical path difference Δ_s. The largest optical path difference is $\Delta_{max} = n_+\Delta_s$.

With this discussion in mind, the specifications for the BPI were chosen as follows. The spectral region was chosen to be 3-5 µm, to cover the important hydrocarbon, carbon dioxide and nitrous oxide absorptions, and other gases in the mid-wave infrared region. Hence, $\lambda_{min} = 3$ µm and $\Delta_{Nyquist} = 1.5$ µm. To maximize Δ_{max}, Δ_s was set equal to $\Delta_{Nyquist}$. Using the rule of thumb described above,

the number of positive interferogram points was set to $n_+ = (1 - 0.25)NM = 0.75 \cdot 80 = 60$. The largest optical path difference then becomes $\Delta_{\max} = 90$ µm, which yields a resolution of $\Delta\tilde{\nu} = 111$ cm^{-1}. The total number of spectral points in the reconstructed spectrum will be $N_{\lambda,\text{tot}} = \Delta_{\max}/\lambda_{\min} = 30$. These points will be evenly spread out in wavenumber space between $\tilde{\nu}_{\min} = 0$ cm^{-1} and $\tilde{\nu}_{\max} = 1/\lambda_{\min} = 3333$ cm^{-1}. Therefore, the number of spectral points in the wavelength region between $\lambda_{\min}$ and $\lambda_{\max} = 5$ µm will be

$$N_\lambda = N_{\lambda,\text{tot}} \frac{1/\lambda_{\min} - 1/\lambda_{\max}}{\tilde{\nu}_{\max} - \tilde{\nu}_{\min}} = 30 \frac{3333 - 2000 \text{ cm}^{-1}}{3333 - 0 \text{ cm}^{-1}} = 12. \tag{4.3}$$

This means that a part of the spectral resolution is wasted on wavelengths that are outside the spectral region of interest, a drawback that is inherent for all conventional interferometers.

γ, δ, prism height and fringe localization plane

With the specifications for the hyperspectral camera already set, the goal was to determine the values of the remaining parameters so that these specifications were met. In practice, this meant finding the optimal combination of parameter values that yielded the predetermined $\Delta_{\max} = 90$ µm. There are several parameters that Δ, and therefore $\Delta_{\max}$, depends on, namely the height of the prisms, the wedge angle γ and the optic axis inclination angle δ. These parameters, in turn, determine the distance between the BPI and the fringe localization plane.

Figure 4.4 illustrates how Δ depends on γ and δ. The two plots show Δ as a function of the x-position of normally incident rays on a BPI of height 15 mm, for different combinations of γ and δ. In Fig. 4.4a, Δ is shown for five different values of γ, while δ is fixed at 70°. In Fig. 4.4b, γ is fixed at 110° and Δ is shown for five different values of δ. There is a general trend of increasing optical path differences with both γ and δ, and a strong linearity over all combinations of the parameters. Additionally, γ has a greater impact on Δ than δ has.

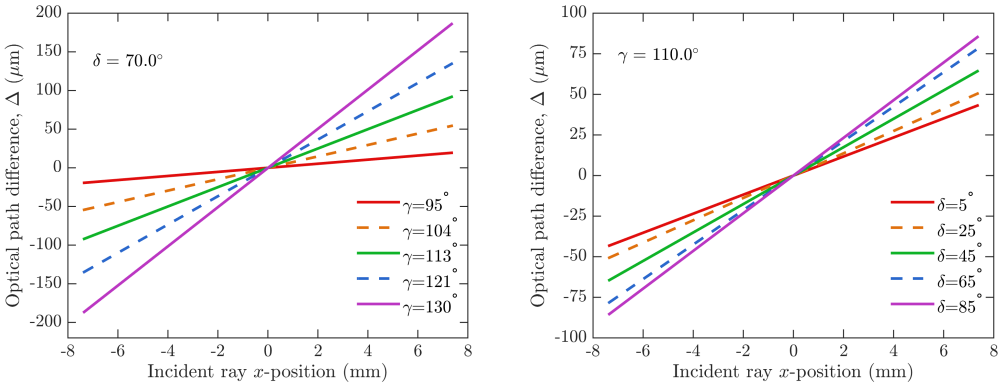

(a) Δ for different values of γ. **(b)** Δ for different values of δ.

Figure 4.4: Optical path difference as a function of x-position of rays at normal incidence on the BPI for different combinations of γ and δ.

Cooled detectors typically have a dewar cooler assembly in front of the pixel array. This means that there is an enclosed volume, typically about 30 mm long, between the pixel array and the entrance window, where no components can be placed. Therefore, the distance between the last component and the pixel array has to be greater than this distance. As stated in Sec. 3.2, a crucial aspect of the BPI design was the placement of the FPA at the fringe localization plane. With a cooled detector placed face to face with the BPI, the distance between the BPI and the fringe localization plane would thus need to be at least 30 mm for the fringe localization plane to coincide with the pixel array. Figure 4.5a shows the distance between the BPI and the fringe localization plane as a function of γ and δ. The maximum distance occurs when $\delta = 35°$ and $\gamma \searrow 90°$ (γ cannot be exactly 90° as this would mean infinitely thin prisms). In Fig. 4.5b, the distance is plotted as a function of prism height for these values of γ and δ. It shows that in order to get a distance of 30 mm, the prism height would need to be at least 150 mm. However, this is larger than the size of the FPA, which was approximately $1280 \cdot 15$ µm $\times$ $1024 \cdot 15$ µm $= 19.2$ mm$\times 15.4$ mm, so all rays would not reach the detector. The solution to this problem was to introduce a relay lens system between the BPI and the FPA which relay the interference fringes and the images from the lenslet array to the FPA. The optical design of the relay lens system is described in Sec. 4.3.With the introduction of the relay lens system, the fringe localization plane no longer have to coincide with the FPA, which means that the position of the plane, and therefore the height of the prisms, γ and δ, can be chosen more freely. Ideally, the fringe

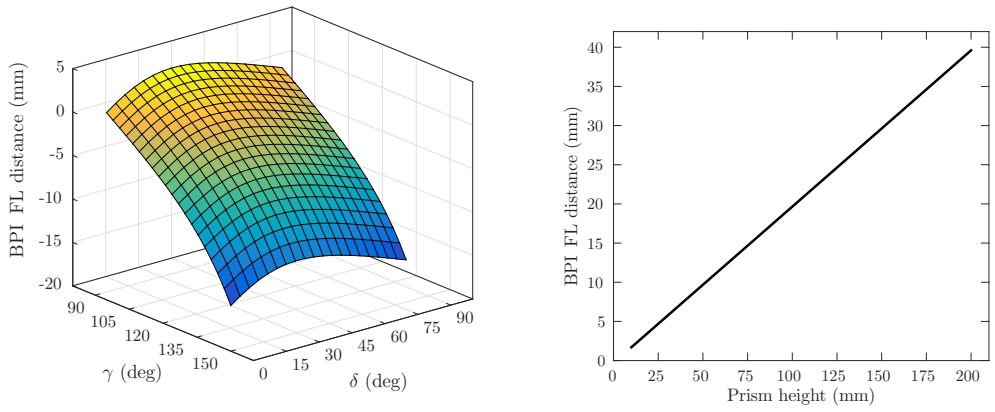

(a) Distance to the fringe localization plane as a function of γ and δ for a prism height of 20 mm. The maximum occurs for $\delta = 35°$ and $\gamma \searrow 90°$ (γ cannot be exactly 90°).

(b) Distance to the fringe localization plane as a function of prism height for $\gamma = 90.1°$ and $\delta = 35°$.

Figure 4.5: Distance between the birefringent polarization interferometer and the fringe localization plane. The figure on the left determines the combination of γ and δ that gives the maximum distance. The figure on the right uses these parameters to show the maximum possible distance as a function of the prism height.

localization plane should be placed outside of any volume, for example prisms, to avoid imaging of any impurities within the volume. Furthermore, it should be placed far away from any optical surfaces to reduce stray light from multiple reflections, and to avoid imaging of dust particles on the surface.

To determine the optimal prism height, wedge angle, optic axis inclination angle, and fringe localization plane distance, so that $\Delta_{\max} = 90$ µm, an initial prism height was selected and rays were traced through the BPI for all combinations of γ and δ. For each simulation where the distance to the fringe localization plane was greater than a predetermined threshold, the largest optical path difference $\Delta_{\max}$ was calculated. If no combination of γ and δ yielded $\Delta_{\max} \geq 90$ µm, the prism height was increased and the simulations repeated. If the largest $\Delta_{\max} \gg 90$ µm, the prism height was instead decreased and the simulations repeated. Finally, if the largest $\Delta_{\max} \approx 90$ µm, the combination of γ, δ, prism height and fringe localization plane distance that gave the value closest to 90 µm was chosen. The results from these simulations are shown in Fig. 4.6, where $\Delta_{\max}$ is plotted as a function of γ and δ for a prism height of 21 mm and a fringe localization plane distance greater than 1 mm. From this plot, $\gamma = 103.8°$ and $\delta = 48.3°$ were chosen, yielding $\Delta_{\max} = 89.98$ µm and a fringe localization plane distance of 1.0 mm.

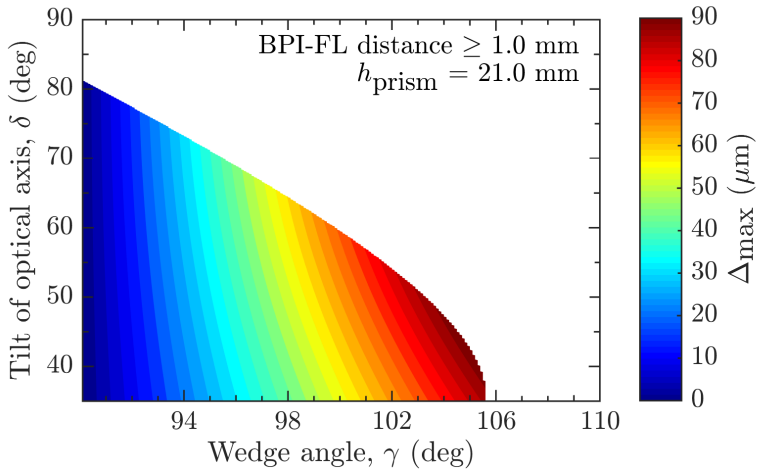

Figure 4.6: $\Delta_{\max}$ as a function of γ and δ for a fringe localization plane distance greater than 1 mm and a prism heigh of 21 mm.

Final design

As can be seen in Fig. 4.4, the optical path difference is zero for $x = 0$ mm, which corresponds to the symmetry axis of the Nomarski prisms, where the two wedges have the same thickness. Above this axis, Δ is positive, and below the axis, Δ is negative. Because only 25 % of the interferogram should sample negative Δ, only 25 % of the prism height needs to be below this symmetry axis and the rest can be above it. To achieve this, the prism wedges can be cut, so that they are truncated,

which saves material that would have otherwise been unutilized. This has been done in the final design, which is shown in Fig. 4.7. The fringe localization plane is 1 mm from the prism back face. The analyzer is moved 2 mm from the prism back face to make room for the fringe localization plane. The low birefringence of sapphire makes the two rays almost indiscernible in the figure, as the paths are almost identical.

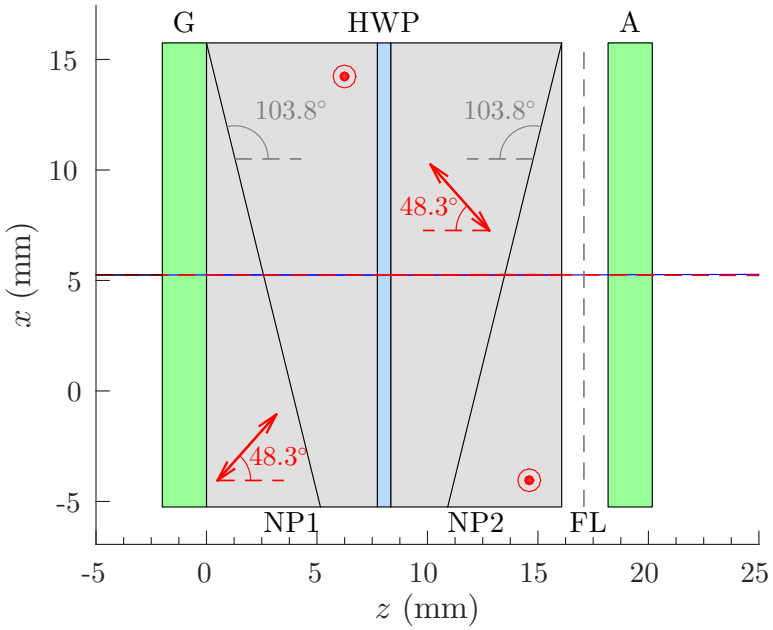

Figure 4.7: Final design of the BPI. The prisms have been truncated and the analyzer has been moved from the prism back face to make room for the fringe localization plane.

4.3 Optical design

The complete snapshot hyperspectral camera system was modelled by building an optical model and integrating it with the BPI model. Like the BPI, the optics was modelled in MATLAB. The purpose of the model was to provide a proof-of-concept simulation showing how the BPI could be combined with auxiliary optics to create a hyperspectral imaging system. Thus, the optical design was more theoretical than a real practical optical design. All lenses were modelled as thin lenses, so optical effects such as aberrations and stray light were not included. These effects could be incorporated, and the optical design refined and improved, with dedicated optical design software such as Zemax. However, this was considered beyond the scope of this thesis.

Optical system design

An overview of the optical model with the final design is shown in Fig. 4.8a. An afocal telescope, consisting of two objective lenses, (OL1) and (OL2), and two baffles, (B1) and (B2), is included at the front of the system to limit the field of view. Both objective lenses have focal ratios of 1 and are placed with a separation of two focal lengths when focused at infinity, so that they share a common focal point between them. The conventional field stop configuration with a single field stop placed in the middle of the two lenses has been replaced by a configuration with two baffles. This is to reduce stray light coming from the baffles themselves and other parts of the system. All components in the system, except the cooled detector, will be at room temperature, and thus emit infrared radiation solely because they are warm. The baffles can be approximated as black bodies, and thus radiate according to Planck's law. At room temperature, a non-negligible fraction of the total energy is emitted in wavelengths that coincide with the spectral response of the detector. By placing the baffles away from the focal point, stray light coming from the baffles, the interior walls of the camera and other components in the system is reduced.

The lenslet array (LA) consists of 10 thin lenses stacked vertically. The diameter of each lenslet is equal to the height of the prisms divided by 10. The angle and x position of each ray incident on the BPI is fed into the BPI model described in Sec. 4.2 to accurately trace the rays through it. For clarity, the figures only show one of the polarizations from the BPI.

A relay lens system, consisting of two lenses, (RL1) and (RL2), relays the images and interference fringes created by the lenslet array and BPI, respectively, to the FPA. A cold shield aperture (CSA), which is mounted in the dewar at a fixed distance from the FPA, insulates the detector from the rest of the system.

The focal length of the lenslets and the distance between the lenslet array and the BPI was adjusted so that the images formed by the lenslets were focused exactly at the fringe localization plane, so that the intermediate image plane was coincident with the fringe localization plane. Furthermore, the focal length and position of RL1 was adjusted so that its focal plane also was coincident with the fringe localization plane, thus relaying both the sub-images and interference fringes. This is shown in Fig. 4.8b. The position and focal length of RL2 were adjusted so that all rays were transmitted through the cold shield aperture. The FPA was positioned at the final image plane, see Fig. 4.8c. The focal length of the lenslets and relay lenses were further adjusted so that the sub-images filled the entire FPA without overlapping, thus maximizing the the number of utilized pixels. Finally, the lenslets were set at $f/7.34$, RL1 at $f/1$ and RL2 at $f/2.3$. The total length of the system was approximately 200 mm.

Incident angle analysis

To determine the dependence of optical path difference on incident angle for the system, rays were traced through the whole system and the optical path difference calculated. First, the rays were required to be normally incident on OL1, which

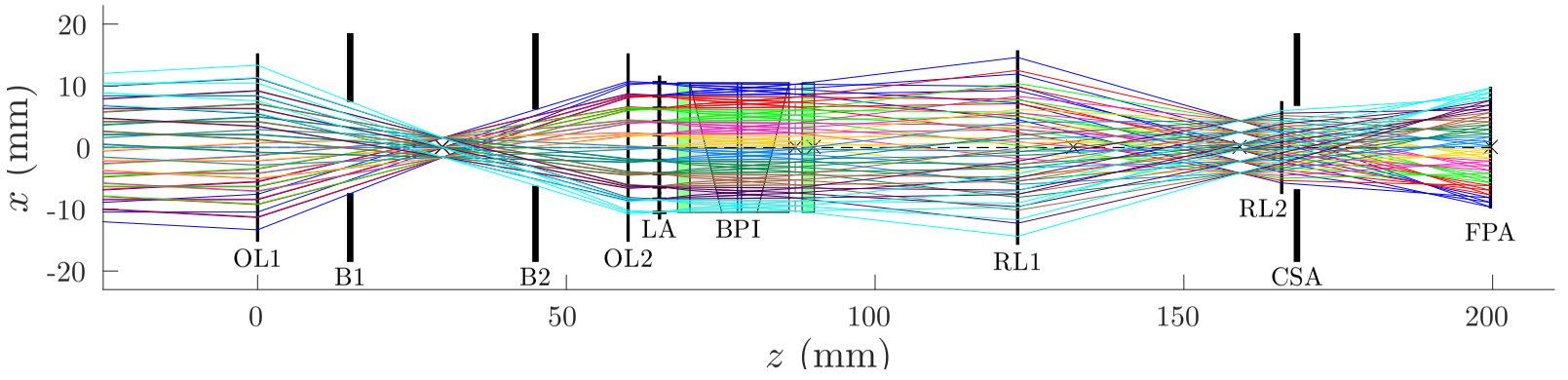

(a) Overview of the full system.

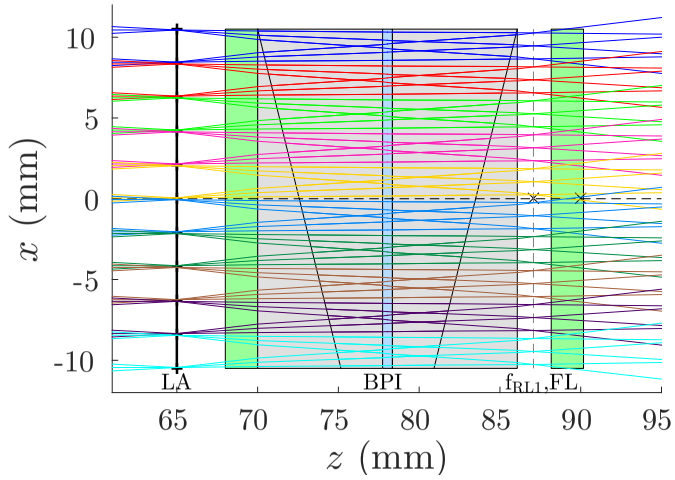

(b) Zoomed in on the BPI and lenslet array. The focal point of RL1, f_{RL1}, coincides with the fringe localization plane FL.

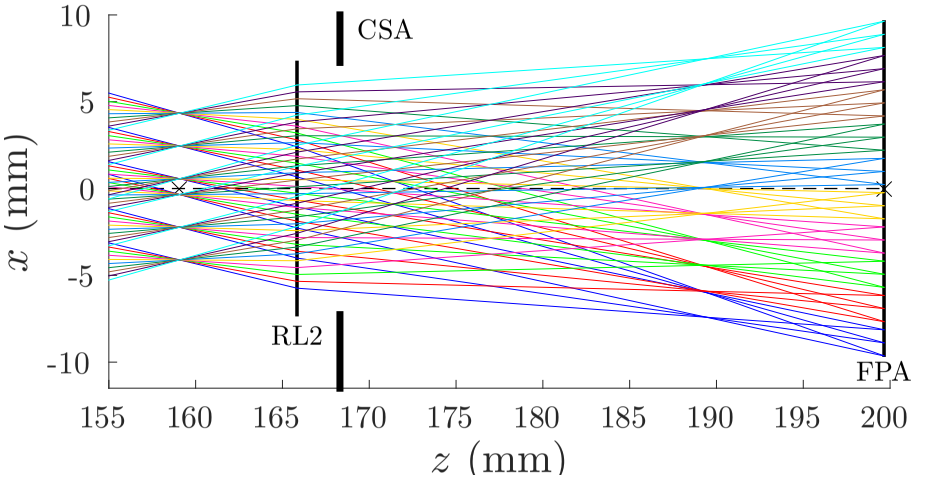

(c) Zoomed in on the cold shield aperture and FPA.

Figure 4.8: The optical model consisting of two objective lenses (OL1) and (OL2), two baffles (B1) and (B2), a lenslet array (LA), the birefringent polarization interferometer (BPI), two relay lenses (RL1) and (RL2), a cold shield aperture (CSA) and the FPA.

means that they were normally incident on the lenslet array as well. Furthermore, all rays were required to go through the same lenslet. For each ray, the incident angle on the BPI and the optical path difference was calculated. The ideal case, and the case the BPI is designed for, is when all rays are normally incident on it. Thus, the figure of interest is the deviation from this case for rays with non-zero incident angle. This is shown in Fig. 4.9a, where the difference in Δ is plotted as a function of incident angle on the BPI. The difference is relatively small compared to the sampling period $\Delta_s = 1.5$ µm, and always less than 15 % of it. The same calculation was repeated for rays incident on OL1 at 5°. The result is shown in Fig. 4.9b. The non-zero incident angle on OL1 makes the angles incident on the BPI larger than in the first case. Hence, the deviations are larger. In this case, the differences can be as large as 30 % of Δ_s. Therefore, the field of view should be restricted to obtain as accurate optical path differences as possible. This is the purpose of the afocal telescope and baffles.

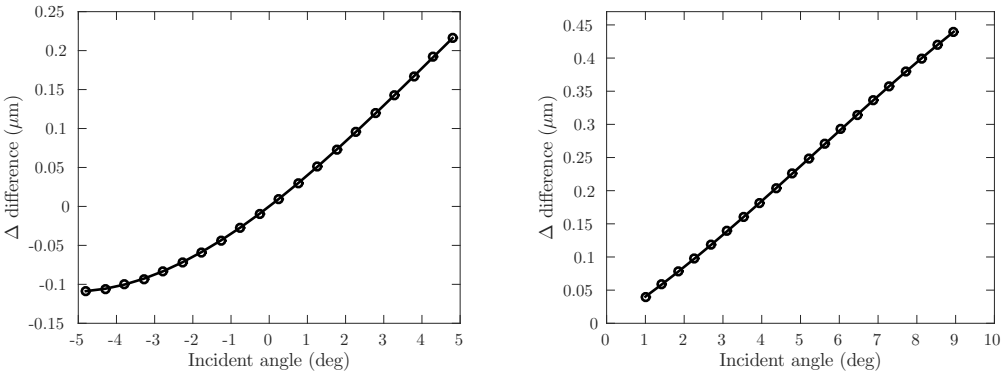

(a) Rays normally incident on system. **(b)** Rays incident on system at 5°.

Figure 4.9: Difference in Δ as a function of incident angle on the BPI. The difference is defined as the optical path difference for the ray minus the optical path difference for a normally incident ray.

Chapter 5

3D Simulations and Spectra

This chapter describes how the full hyperspectral imaging system was modelled in 3D, and how it was used to simulate interferograms and spectra. The chapter begins with a description of how the interferometer model was extended to three dimensions, and how this model was used to simulate idealized interferograms and spectra. This is followed by a description of the optical model in three dimensions, and how the optical model and the interferometer model was combined to a model of the full hyperspectral imaging system. Finally, this model is used to simulate a few interferograms and spectra.

5.1 3D interferometer model

The 2D interferometer model described in Ch. 4 could only simulate rays incident in the zx-plane. To be able to simulate all incident rays, the 2D model was extended to 3D. The simulation algorithm used for the 2D model (see Fig. 4.2) was also used for the 3D model, but with necessary generalizations to add the third dimension.

The ray tracing calculations in Sec. 3.1 were valid when the incident plane, defined by the incident wave vector $\hat{\mathbf{k}}_1$ and the surface normal $\hat{\mathbf{n}}$, was coincident with the xy-plane, $\hat{\mathbf{n}}$ was parallel to the x-axis, and the yz-plane was coincident with the surface of the prism (see Fig. 3.1). In the 2D model, this was automatically fulfilled, albeit with different names of the axes, i.e. the incident plane was the zx-plane, $\hat{\mathbf{n}}$ was parallel to the z-axis, and the xy-plane was coincident with the surface of the prism. At the slanted wedge intersections, the wedge angle could simply be added or subtracted from the incident and refracted angles to correct for the normal not being parallel to the z-axis. This formally meant that the calculation was carried out in a new coordinate system $x'y'z'$ that was rotated about the y-axis to align the z'-axis with the surface normal. After the calculation, the system was rotated back and the angles in the original xyz-system could be used for subsequent calculations. The same method was used to calculate rays incident with a non-zero y-component in the 3D model. Here, the coordinate system was rotated to align the $z'x'$-plane with the incident plane, with the z'-axis parallel to the surface normal.

The calculations were carried out in the rotated coordinate system, after which everything was rotated back to the original xyz-system for subsequent calculations.

Equation 4.1 for the optical path length was naturally generalized to three dimensions,

$$\begin{aligned} L = &\sum_{i=1}^{4} n_i \sqrt{(z_{i+1} - z_i)^2 + (x_{i+1} - x_i)^2 + (y_{i+1} - y_i)^2} \\ &+ \operatorname{sgn}(z_{\mathrm{FL}} - z_5) n_5 \sqrt{(z_{\mathrm{FL}} - z_5)^2 + (x_{\mathrm{FL}} - x_5)^2 + (y_{\mathrm{FL}} - y_5)^2}. \end{aligned} \tag{5.1}$$

As described in Sec. 3.3, the BPI is rotated an angle ψ about the z-axis to make the optical path difference dependent on both x and y. To make the sampling period constant between each sampling point, Δ needs to vary linearly between each subsequent sub-image,

$$\Delta(x_{i+1}, y_{i+1}) - \Delta(x_i, y_i) = \Delta_{\mathrm{s}} \; \forall i \in \{1, 2, N \times M - 1\}. \tag{5.2}$$

Because Δ is linear in x (see Fig. 4.4), this is achieved when $\psi = -\arctan(1/M)$, where the minus sign makes Δ decrease with y instead of increase . With $M = 8$, as determined in Sec. 4.2, $\psi = -7.125°$.

Ideal simulations

Using the 3D interferometer model, ideal interferograms and spectra were simulated. The 3D model and the rays used to simulate the interferogram are shown in Fig. 5.1. There were 10×8 equidistant rays in a rectangular grid with a spacing of 2.1 mm, corresponding to the diameter of the lenslets. All rays were normally incident on the BPI. The setup simulates the case where rays normally incident on the lenslet array go through the center of each lenslet. The intererogram resulting from this simulation is an ideal one, in the sense that all rays are normally incident on the BPI, so the effect of incident angle on Δ, which would be present when operated in normal conditions, is neglected. The 80 optical path differences from this simulation had a minimum of $\Delta_{\min} = -32.5$ µm, a maximum of $\Delta_{\max} = 90.0$ µm, and a mean sampling period of $\Delta_{\mathrm{s}} = 1.55$ µm with a standard deviation of $2.71 \cdot 10^{-10}$ µm.

Using the same set of 80 optical path differences, different sources were simulated to generate different interferograms. The interferograms were calculated using Eq. 3.18, with $I(\tilde{\nu})$ equal to some source spectrum function.

In Fig. 5.2a, the source is a black body, so $I(\tilde{\nu})$ is Planck's law,

$$I(\tilde{\nu}) = B(\tilde{\nu}, T) = 2hc^2\tilde{\nu}^3 \frac{1}{\mathrm{e}^{hc\tilde{\nu}/k_{\mathrm{B}}T} - 1}, \tag{5.3}$$

where h is Planck's constant, c is the speed of light, k_{B} is Boltzmann's constant, and T is the temperature, which in this case was set to $T = 300$ K. The source spectrum was normalized prior to calculating the interferogram. The spectrum was reconstructed using the Cooley-Tukey fast Fourier transform algorithm [34]. This

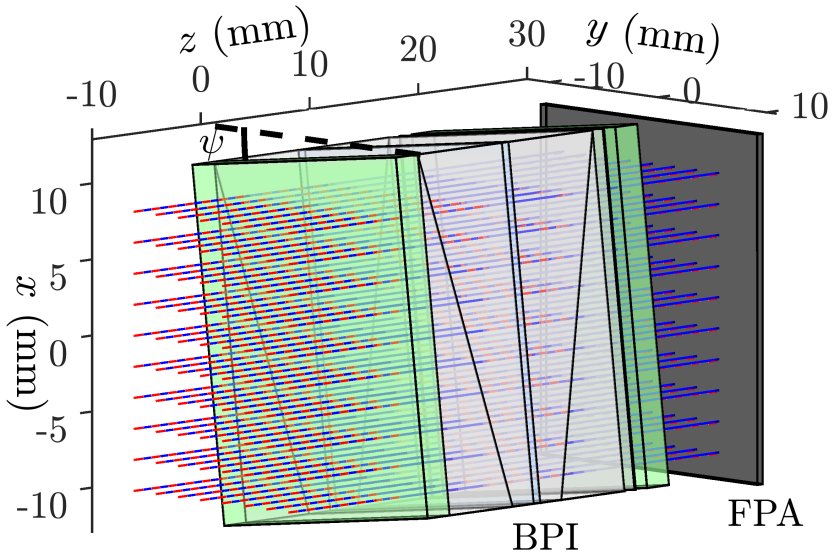

Figure 5.1: 3D model of the birefringent polarization interferometer built in MATLAB.

algorithm requires that the number of sample points is a power of two. Therefore, a standard zero-filling procedure of the interferogram was performed to increase the number of points from 80 to the nearest power of two, $2^7 = 128$. This increase in the number of points in the spectrum gives an apparent smaller $\Delta\tilde{\nu}$, i.e. an apparent higher resolution. However, the added zeros do not add any new information, zero-filling has the effect of interpolating the spectrum. Thus, the effective resolution is based on the number of sample points prior to zero-filling. Figure 5.2b shows the reconstructed spectrum overlayed on the original black body source spectrum for 3–5 µm. The reconstruction is very accurate and is practically indistinguishable from the original spectrum.

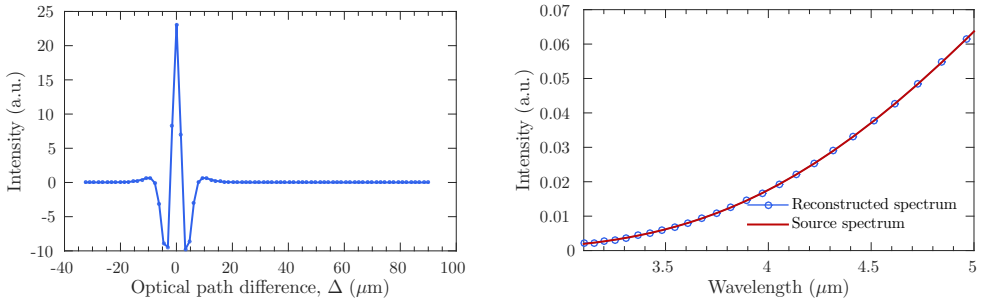

(a) Interferogram. **(b)** Source and reconstructed spectrum.

Figure 5.2: Simulated interferogram and reconstructed spectrum of a black body source at 300 K.

Figure 5.3 shows the reconstruction of a source of two closely spaced monochromatic lines. The spacing is equal to the theoretical resolution $\Delta\tilde{\nu} = 111$ cm^{-1}, which

at 3.3 µm corresponds to 0.13 µm. The reconstructed peaks are partly overlapping, but the two lines can still be resolved, affirming that the theoretical prediction for the resolution is quite accurate. Thus, spectral lines closer than about 111 cm^{-1} will not be resolved.

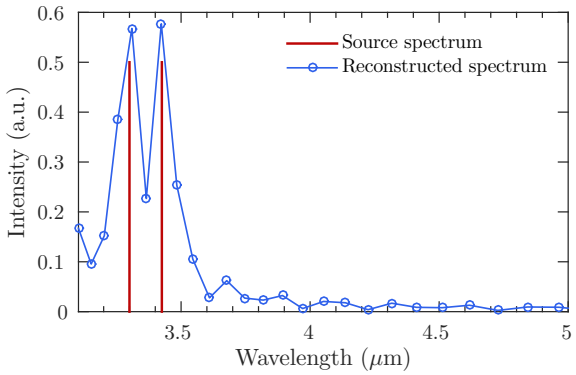

Figure 5.3: Reconstruction of two monochromatic lines at 3.3 µm and 3.43 µm, corresponding to the theoretical resolution of $\Delta\tilde{\nu} = 111$ cm^{-1}.

The hyperspectral camera is primarily designed to detect and identify gases with absorption in the 3–5 µm band. To test the interferometers ability to do that, absorption spectra of five different gases, methane (CH_4), ethene (C_2H_4), butane (C_4H_{10}), carbon dioxide (CO_2) and nitrous oxide (N_2O), were reconstructed. The gas spectra were generated with Hitran-PC 4.2 [35], with a resolution of 0.1 cm^{-1}, a Lorentzian lineshape, a temperature of 296 K, and a concentration times path length of 1000 ppmm. The gas spectra and reconstructions are shown in Fig. 5.4. The reconstruction of the methane spectrum (Fig. 5.4a) is rather inaccurate. The rapidly varying spectrum, with the large number of closely spaced sharp peaks, is difficult to reconstruct with the relatively low resolution of the interferometer. The reconstruction only seems to produce a small bump where the absorption peaks are. This can be understood by studying the average intensity of the source spectrum, shown as the black curve. The averages are taken for intervals centered on each sample point and of a length equal to the inter-sample distance. The absorption peaks are so sharp that the averages always are close to the baseline. In fact, the reconstructed spectrum quite accurately follows the average intensity line, which is why the methane spectrum reconstruction only generates a bump, rather than a more accurate rendition. Ethene is slightly heavier than methane and its spectrum therefore not quite as rapidly varying (Fig. 5.4b). However, the peaks are still very sharp and closely spaced in comparison with the resolution of the interferometer, which is reflected in the reconstruction which also was quite inaccurate. The reconstruction of the butane spectrum is more accurate (Fig. 5.4c). The butane spectrum is not as rapidly varying as that of the lighter hydrocarbons, so the reconstructed spectrum follows it much more accurately. The same is true for carbon dioxide (Fig. 5.4d) and nitrous oxide (Fig. 5.4e), whose reconstructed spectra both were relatively accurate.

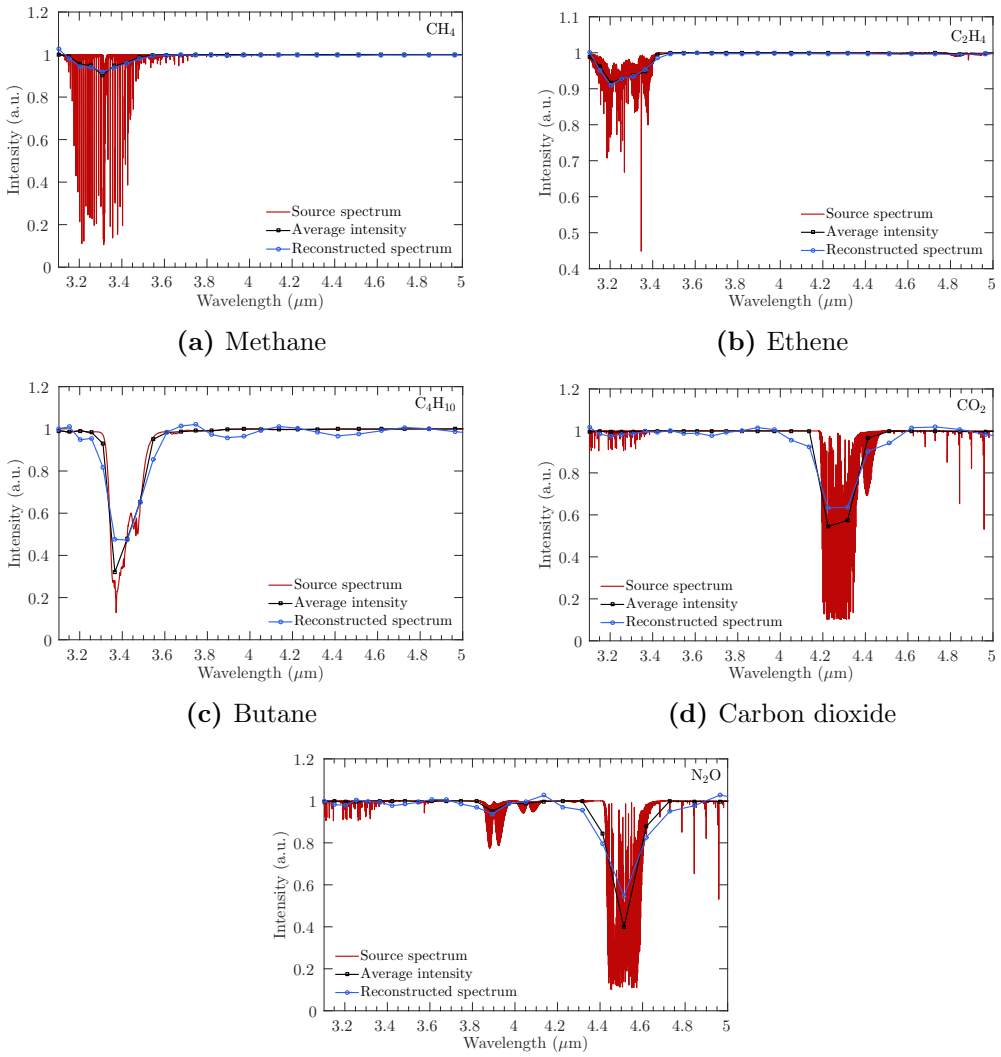

(a) Methane **(b)** Ethene

(c) Butane **(d)** Carbon dioxide

(e) Nitrous oxide

Figure 5.4: Reconstructions of five different gas spectra: methane, ethene, butane, carbon dioxide and nitrous oxide. The black line is the average intensity of the source spectrum at each sample point, calculated for intervals of the same length as the inter-sample distance, centered on each sample point.

The interesting question is whether the different gas spectra could be distinguished from each other, in order to possibly identify them in real applications. Figure 5.5 shows the five reconstructed gas spectra overlaid. Butane, carbon dioxide and nitrous oxide are clearly distinguishable from each other, and also distinguishable from the two lighter hydrocarbons, methane and ethene. Methane is the main component of natural gas. During the processing to purify raw natural gas, butane appears as a by-product. During a leak it is very valuable to be able to distinguish between these hazardous gases, in order to determine the extent and position

of them. Butane can clearly be identified and also distinguished from methane. However, because the reconstructed methane spectrum is so different from a real methane spectrum, it is questionable whether it could be recognized. Especially considering that the methane bump is not much larger than the residual side lobes of the butane spectrum at 3.9 µm and 4.4 µm. Ethene is used to produce the plastic polyethylene. Because ethene is hazardous, it is important to detect and identify leaks of it. However, similarly to methane, the reconstructed ethene spectrum is so different from a real ethene spectrum, it is debatable whether it could be recognized. Thus, ethene could probably be detected but not identified. Carbon dioxide appears as a by-product in both natural-gas processing and polyethylene processing. Furthermore, carbon dioxide also appear in all combustion reactions and processes. Therefore, it is desirable to distinguish carbon dioxide from other gases in many different applications. For example, extracting the carbon dioxide contribution in a large gas cloud to enable the detection of other gases in the cloud. Carbon dioxide is clearly distinguishable from the other gases, so the hyperspectral camera should be useful in a large number of applications. Nitrous oxide is commonly used in surgery and dentistry as an anaesthetic and analgesic. To assure the health and safety of health care professionals, leaking nitrous oxide masks should be detected quickly. This usually means being able to distinguish between nitrous oxide and the carbon dioxide in exhaled air. These gases can clearly be detected and distinguished from each other.

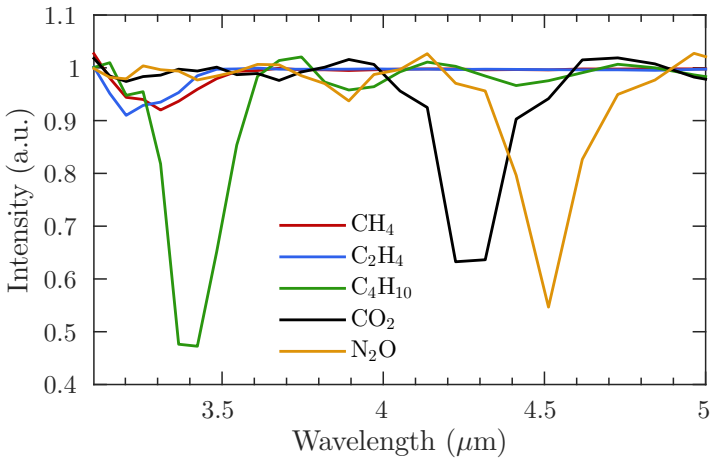

Figure 5.5: Comparison of reconstructed gas spectra.

5.2 3D system model

To be able to simulate the complete system, and to simulate less idealized interferograms and spectra, a 3D model of the full hyperspectral camera system was constructed. The model is depcited in Fig. 5.6. The simulations were implemented

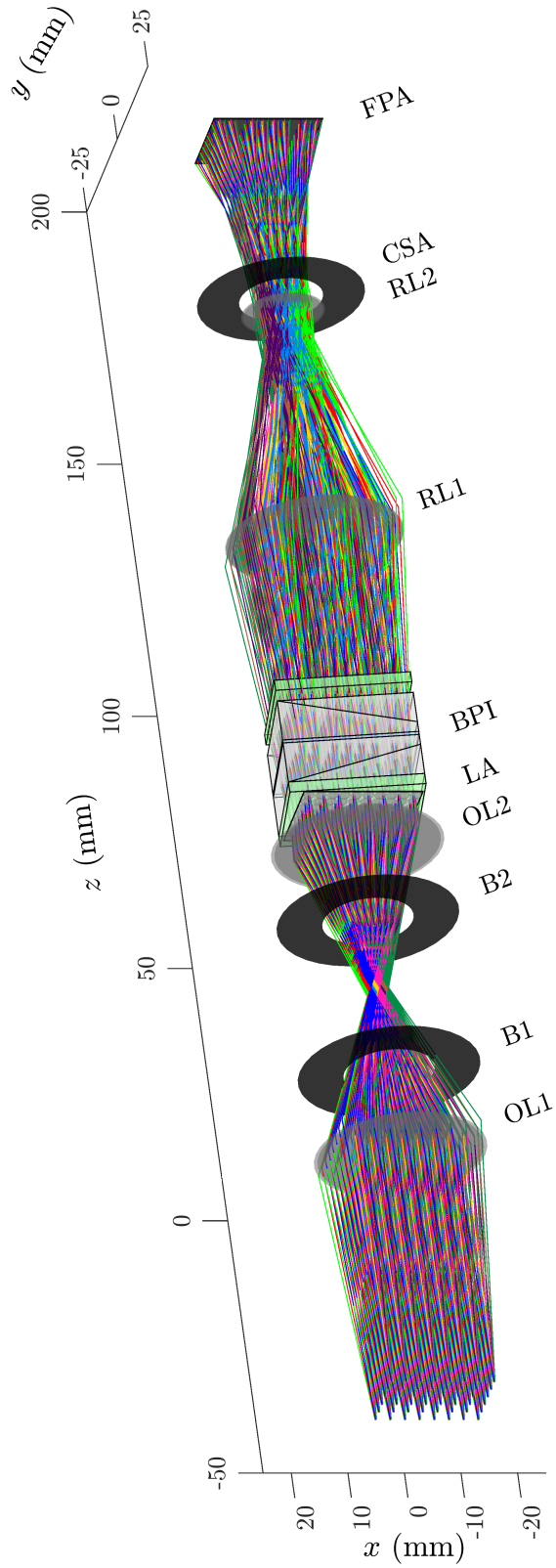

Figure 5.6: 3D simulation model of the hyperspectral imaging system. The simulations were implemented as a two-step process, where the first step was to trace all rays through the system without the BPI, and the second step was to calculate the optical path difference for each ray using the 3D interferometer model described in Sec. 5.1.

as a two-step procedure. In the first step, ray tracing was performed from some object to the FPA, but without the BPI in the system. The optical model described in Sec. 4.3 was extended to 3D. The lenses were modelled as thin lenses and all parameters from the 2D model were left unchanged. The second step was to simulate the rays through the BPI. For each ray in the first step, the intersection with the BPI and the incident angles were fed into the 3D interferometer model described in Sec. 5.1, and the optical path difference calculated. After both simulation steps, the position on the FPA, the corresponding position on the object, and the optical path difference was known for each ray.

The image formation capability of the optical system was analyzed by performing the first step in the simulation, i.e. by tracing rays from an object to the FPA. The object consisted of a grayscale image of a sunflower, shown in Fig. 5.7. The image

Figure 5.7: Object used for image formation simulation.

had a resolution of 128×128 pixels, a height and width of 50 mm, and was placed 1000 mm from the first objective lens. Because the system originally was designed with infinity focus, it had to be refocused to 1000 mm. This was done by moving the second objective lens in the positive z direction until rays from the same point on the object intersected on the FPA. All source points were set to emit rays uniformly and isotropically, and all rays from the same source point were given the same intensity value, corresponding to the intensity in the grayscale image. The number of rays per solid angle was adjusted so that all of the pixels on the FPA (except the pixels constituting the boundaries between sub-images) would get hit at least once, which occurred when each source point emitted $2.4 \cdot 10^5$ rays/sr. Thus, on average 170 rays hit the first objective lens and entered the system. Hence, approximately $128 \times 128 \times 170 \approx 2.8 \cdot 10^6$ rays were simulated through the system. The FPA was assumed to have a fill factor of 1, and the pixels a pitch of 15 µm. The resultant view on the FPA is shown in Fig. 5.8. There are clearly 10×8 sub-images with well-defined boundaries without any overlap. The sub-images are inverted because there are an odd number of lenses in the system. The fact that all sub-images form on the FPA shows that the optical design of the hyperspectral imaging system is correct, and that there is a one-to-one mapping between the object and the pixels of each sub-image.

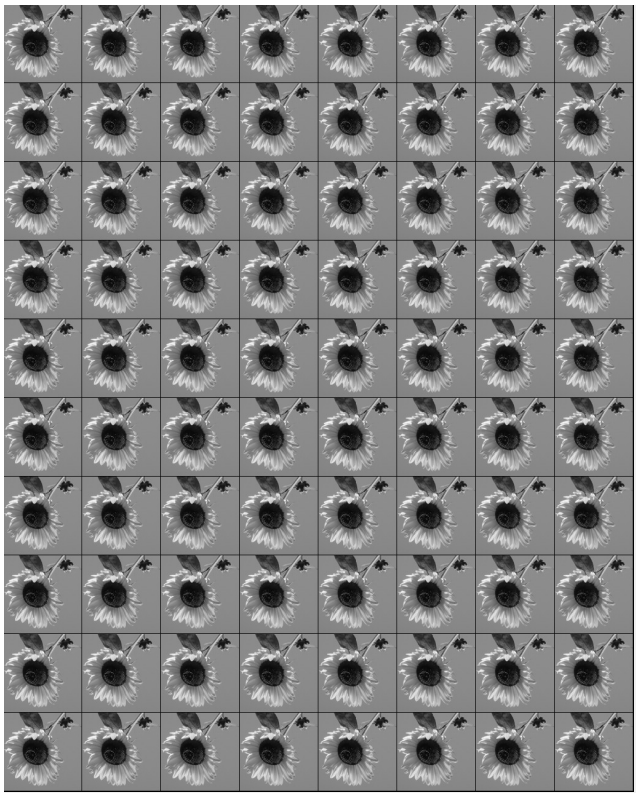

Figure 5.8: Resultant view of the FPA from simulation of image formation.

5.3 Simulated interferograms and spectra

The image formation simulation described in Sec. 5.2 was expanded to include simulation of the BPI, so the optical path difference was calculated for each ray in the simulation. By using different spectra for the source, different interference patterns were recorded on the FPA. Figure 5.9 depicts the recorded intensities on the FPA when the sunflower is imaged and all source points emit the same spectrum as the source in Fig. 5.3, i.e. two monochromatic spectral lines. The sunflower sub-images can still be observed, but they are modulated by the interference pattern resulting from the inclusion of the BPI, which create optical path differences.

There is a repeated pattern of smaller rectangles within each sub-image. These are artifacts, unphysical errors resulting from the implementation of the simulation. They arise as a consequence of the relatively low number of simulated rays. Each source point emitted roughly 170 rays that entered the system. Thus, each vertical slice contained approximately $\sqrt{170} \approx 13$ rays from each source point. Beacuse there were 10 lenslets per column, most of the lenslets were hit by only one ray from each source point. Shown on the x-axis of Fig. 5.10 are the pixels of the same column for one of the sub-images. For each of these pixels, the corresponding ray's intersection with the lenslet minus the center point of the lenslet, is shown

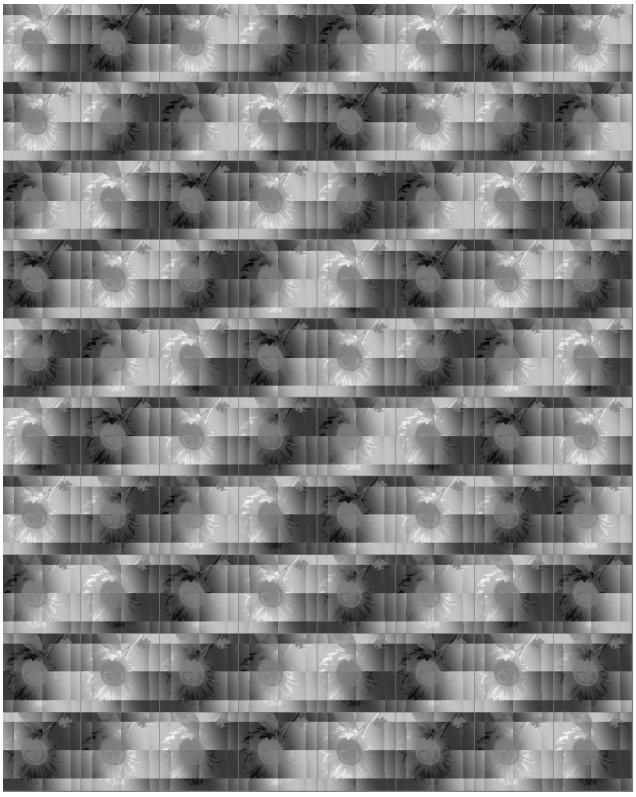

Figure 5.9: View of the FPA when imaging the sunflower through the full hyperspectral camera system, with a source consisting of two monochromatic spectral lines.

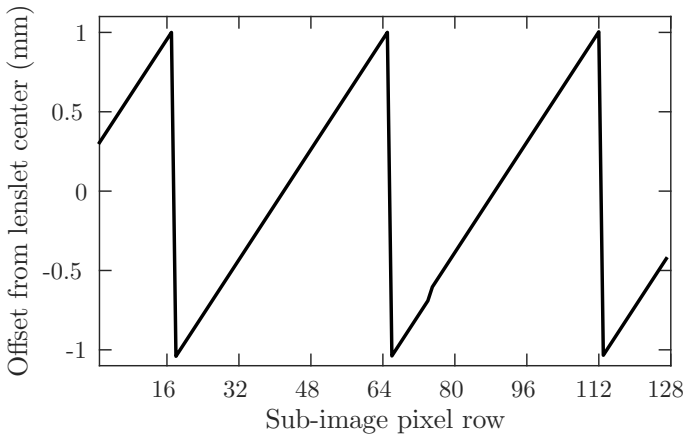

Figure 5.10: Offset from center of lenslet to ray intersection point with lenslet for each pixel in column number 5 in sub-image number 1 (top-left sub-image in Fig. 5.9).

on the y-axis. Hence, the y-axis shows the distance from the center of the lenslet to the intersection point. Noticeable are the large jumps between large positive offset (top of lenslet) to large negative offset (bottom of lenslet) at pixel rows 18, 66 and 113. A comparison with Fig. 5.9 shows that the these rows correspond to the boundaries between the artifact rectangles, as the boundaries approximately are 1/8 of the sub-image width from the edges of each sub-image, and in the middle of them. The large jumps result in a discontinuous optical path difference at these boundaries, which explains the artifacts. In real-world operation of the camera, this discontinuity would of course not be present, as infinitely many rays would go through each lenslet.

Interferograms and spectra were simulated using the full system model. By doing this, the idealized setup in Sec. 5.1 was replaced by a more realistic situation, where the incident angles varied. Each point source yields an individual interferogram and reconstructed spectrum. The qualitative shape of the reconstructed spectrum is the same for all pixels. For the remainder of the chapter, all interferograms and spectra are for one of these source points, pixel $(95, 95)$ in the sunflower image (Fig. 5.7). This arbitrarily chosen point corresponds to a point roughly in the center of the top-right quadrant of the image. The 80 optical path differences had a minimum of $\Delta_{\text{min}} = -35.0$ µm, a maximum of $\Delta_{\text{max}} = 91.0$ µm, and a mean sampling period of $\Delta_{\text{s}} = 1.59$ µm with a standard deviation of $2.08 \cdot 10^{-2}$ µm. It is apparent that the simulation in Sec. 5.1 was idealized, as the standard deviation was eight orders of magnitude smaller compared to this case when the incident angles varied.

The 300 K black body interferogram and spectrum is show in Fig. 5.11a and 5.11b, respectively. The fit is not as good as that in Fig. 5.2b, but is still quite accurate. A possible application of this could be to eliminate the need to manually set the emissivity of the source when performing optical gas imaging. In the absence of gas absorption, a measured deviation from the expected black body spectrum at the known temperature could be attributed to the emissivity of the object.

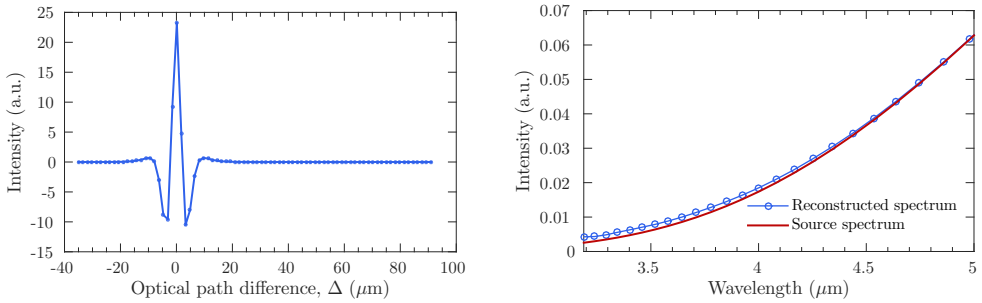

(a) Interferogram. **(b)** Source and reconstructed spectrum.

Figure 5.11: Simulated interferogram and reconstructed spectrum of a black body source at 300 K.

The reconstruction of the two monochromatic lines with a spacing equal to the theoretical resolution of $\tilde{\nu} = 111$ cm^{-1} is shown in Fig. 5.12. The peaks are less

separated and defined than in Fig. 5.3, but are still discernible. Therefore, the spectral resolution of the hyperspectral camera system seems to be equal to the theoretical resolution in this more realistic setup as well.

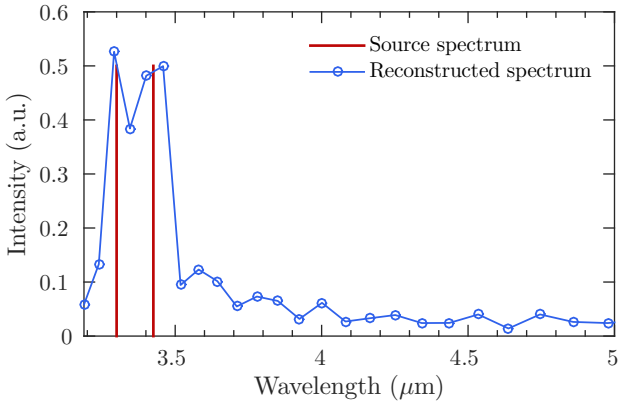

Figure 5.12: Reconstruction of two monochromatic lines at 3.3 µm and 3.43 µm, corresponding to the theoretical resolution of $\Delta\tilde{\nu} = 111$ cm^{-1}.

The gas spectra reconstructions are shown in Fig. 5.13. Because the sampling period was $\Delta_s = 1.59$ µm, the smallest reconstructed wavelength is $2 \cdot 1.59 = 3.18$ µm. This is slightly larger than the aim of 3 µm. To optimize the design further, the full 3D model simulations could be used to determine the interferometer parameters so that the sampling period is closer to 3 µm. Because the shortest reconstructed wavelength was 3.18 µm, the lower lower part of the methane and ethene peaks were not reconstructed. Apart from this, all five reconstructions are similar to the ideal reconstructions in Fig. 5.4.

The gas spectra are shown overlaid in Fig. 5.14. Butane, carbon dioxide and nitrous oxide are clearly distinguishable from each other in this more realistic setup as well, and also distinguishable from the two lighter hydrocarbons, methane and ethene. But, as noted for Fig. 5.5, it is debatable whether the methane spectrum and ethene spectrum could be identified at all, because they are so different from a their real spectra.

The results seem to indicate that the hyperspectral imaging system could be used for optical gas imaging. Certain gases could be detected *and* identified, e.g. butane, carbon dioxide and nitrous oxide, as shown by the reconstructed spectra in this chapter, as well as other gases with moderately varying absorption spectra in the 3-5 µm band. However, gases with more rapidly varying spectra have been shown to be difficult to reconstruct. These gases, most notably methane and ethene, might be problematic to identify with this system. By improving the spectral resolution of the camera, it is possible that this could be rectified.

The most obvious way to increase the spectral resolution is to increase the number of sub-images and thus sample points. However, if the detector resolution is fixed, this would decrease the spatial resolution. A small increase in spectral resolution could be achieved by making the interferograms more single-sided. However,

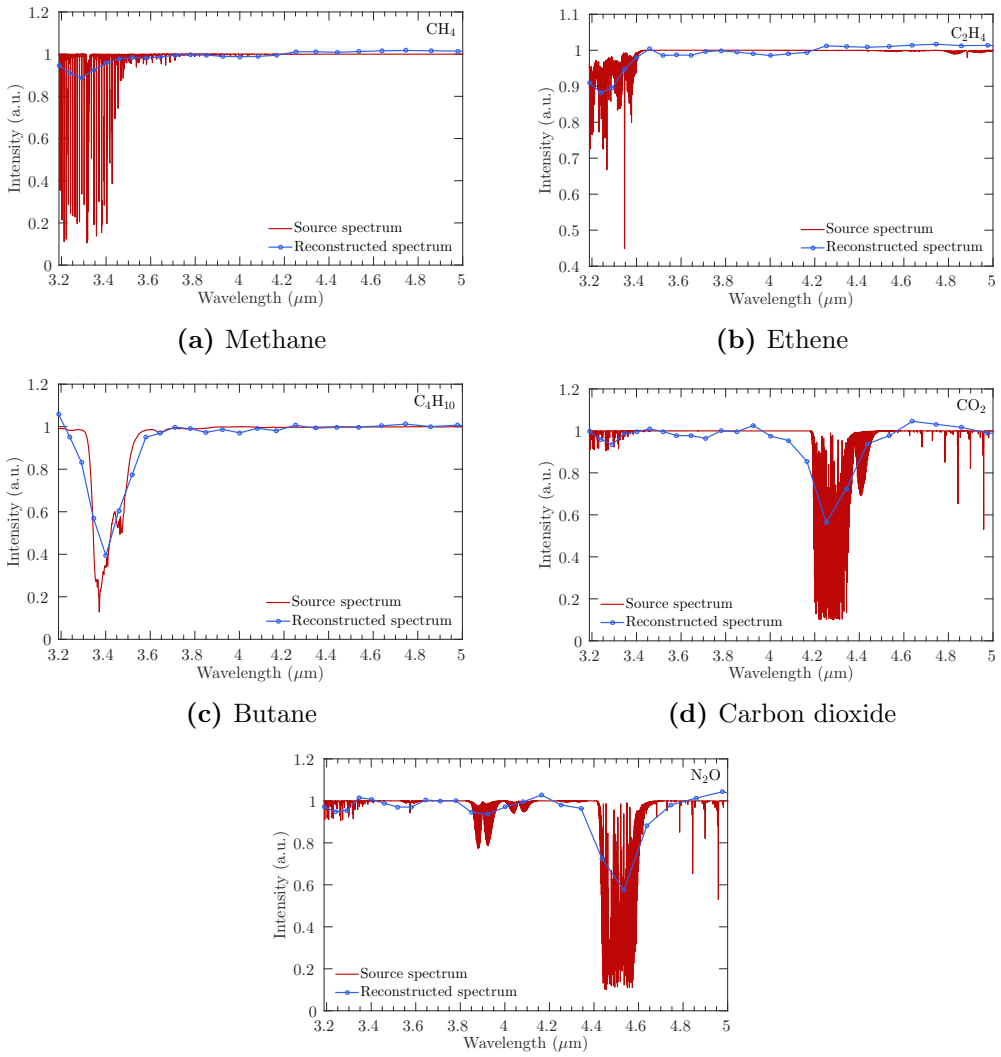

(a) Methane

(b) Ethene

(c) Butane

(d) Carbon dioxide

(e) Nitrous oxide

Figure 5.13: Reconstructions of five different gas spectra: methane, ethene, butane, carbon dioxide and nitrous oxide.

this would have to be weighed against potential phase-errors that might arise when the interferograms become too single-sided.

A third approach would be to employ a technique called spatial heterodyning [36]. This requires additional components in the system: a quarter-wave plate and a polarization grating. These components introduce a wavenumber dependence in the optical path difference, giving an offset in the interferogram,

$$I(\Delta) = \int_0^\infty I(\tilde{\nu})(1 + \cos(2\pi\Delta(\tilde{\nu} - \tilde{\nu}_0)))\mathrm{d}\tilde{\nu}, \tag{5.4}$$

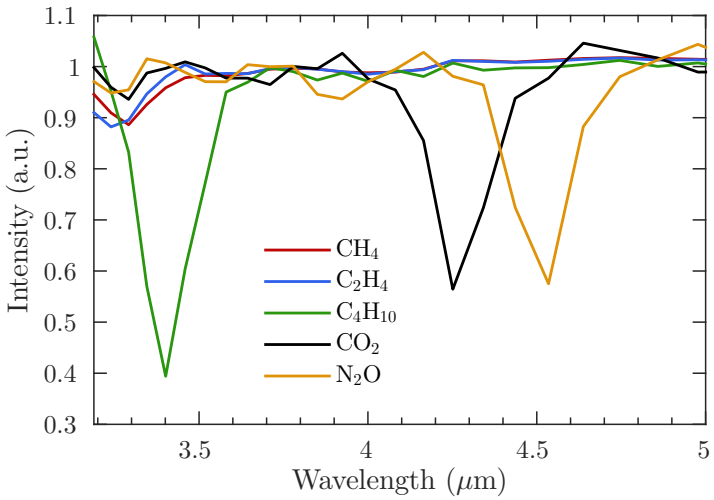

Figure 5.14: Comparison of reconstructed gas spectra.

where $\tilde{\nu}_0$ is the offset, determined by the characteristics of the polarization grating. As mentioned in Sec. 4.2, the interferogram sampling points are evenly spread out in wavenumber space between $\tilde{\nu}_{\text{min}}$ and $\tilde{\nu}_{\text{max}} = 1/\lambda_{\text{min}}$. For the interferometer described in this thesis, $\tilde{\nu}_{\text{min}} = 0$ cm^{-1}. Hence, all samples between 0 cm^{-1} and $1/\lambda_{\text{max}}$ is effectively wasted, because they are outside the wavelength region of interest. However, with the offset $\tilde{\nu}_0$, the minimum wavenumber can be shifted to minimize the number of samples outside the region of interest. By selecting $\tilde{\nu}_0 = 1/\lambda_{\text{max}}$, all samples would be within the region of interest. For example, instead of roughly 12 samples between 3-5 µm as for the interferometer described in this thesis, all $N_{\lambda,\text{tot}} = 30$ samples would be within this band.

Chapter 6

Summary and Conclusions

A hyperspectral technology based on birefringent prisms, originally designed for surveillance and target identification in unmanned vehicles in the visible spectrum, has been adapted to optical gas imaging applications in the mid-wave infrared. The instrument is snapshot, eliminating the risk of scanning artifacts when imaging dynamic scenes. The instrument was optimized to operate in the 3-5 µm range, targeting the hydrocarbon gases, as well as carbon dioxide and nitrous oxide. An optical design with relay lenses was incorporated to adapt the instrument to use a cooled detector. The particular implementation of the instrument described in the thesis produces 80 sub-images with a spatial resolution of 128×128 pixels and a spectral resolution of approximately 110 cm^{-1}.

A couple of different spectra were reconstructed with a simulation model that was built of the system. Five different gas spectra were simulated, methane, ethene, butane, carbon dioxide and nitrous oxide. The butane, carbon dioxide and nitrous oxide spectra could be reconstructed quite accurately, whereas the methane spectrum and ethene spectrum reconstructions were rather different from the real spectra. The inability to reconstruct methane and ethene accurately was due to the low spectral resolution in comparison with the small width of the sharp peaks in these spectra. The butane, carbon dioxide and nitrous oxide spectra, which are not as rapidly varying as that of the lighter hydrocarbons, could therefore be reconstructed much more accurately.

The aim of the thesis was to find a hyperspectral technology suitable for optical gas imaging. The analysis and results seem to suggest that the investigated technology is suited for optical gas imaging of certain gases. The successful reconstructions of butane, carbon dioxide and nitrous oxide, suggest that gases with moderately varying spectra could be detected and identified. However, it is questionable whether gases with rapidly varying spectra, such as methane and ethene, could be detected and identified. An increased spectral resolution, which could be achieved by increasing the number of sub-images, would improve the reconstructions and possibly increase the number of detectable and identifiable gases.

The successful reconstructions of black body spectra suggest that the instrument could provide more general usages as well. For example, spectrally resolved

reflectance and emissivity estimation of surfaces, which could eliminate the need to manually set the emissivity of the source when operating infrared cameras.

An improved signal-to-noise ratio is expected from this interferometer-based instrument compared to filter-based or dispersive technologies. However, this was not investigated in the thesis. A future signal-to-noise ratio analysis is needed to determine the gas quantification capabilities of the instrument.

Because the model built in this thesis is of a more theoretical nature, using thin lenses and neglecting optical effects such as aberrations and stray light, a more refined and practical optical design is needed. This work has already commenced at FLIR System in Sweden, where a model of the system is being built with the dedicated optical design software Zemax. Future work would then be to use the updated design from the Zemax model and build a proof-of-concept prototype to test the instrument in practice.

Bibliography

[1] J. A. Herweg, J. P. Kerekes, O. Weatherbee, D. Messinger, J. van Aardt, E. Ientilucci, Z. Ninkov, J. Faulring, N. Raqueño, and J. Meola. SpecTIR hyperspectral airborne Rochester experiment data collection campaign. *Proc. SPIE*, 8390:839028, 2012.

[2] B. Zhang, D. Wu, L. Zhang, Q. Jiao, and Q. Li. Application of hyperspectral remote sensing for environment monitoring in mining areas. *Environmental Earth Sciences*, 65(3):649–658, 2012.

[3] L Gao, R. T. Kester, and T. S. Tkaczyk. Compact Image Slicing Spectrometer (ISS) for hyperspectral fluorescence microscopy. *Optics Express*, 17(15):12293, 2009.

[4] E. K. Hege, D. O'Connell, W. Johnson, S. Basty, and E. L. Dereniak. Hyperspectral imaging for astronomy and space surveillance. *Proc. SPIE*, 5159:380–391, 2004.

[5] R. T. Kester, C. Walker, and N. Hagen. A real-time gas cloud imaging camera for fugitive emission detection and monitoring. In *Imaging and Applied Optics Technical Digest*, page AW1B. Optical Society of America, 2012.

[6] N. Hagen, R. T. Kester, and C. Walker. Real-time quantitative hydrocarbon gas imaging with the gas cloud imager (GCI). In *SPIE Defense, Security, and Sensing*, page 83581J. International Society for Optics and Photonics, 2012.

[7] J. Sandsten, P. Weibring, H. Edner, and S. Svanberg. Real-time gas-correlation imaging employing thermal background radiation. *Optics Express*, 6(4):92–103, 2000.

[8] M. Vollmer and K.-P. Möllmann. *Infrared thermal imaging: fundamentals, research and applications*. John Wiley & Sons, 2010.

[9] N. Hagen and M. W. Kudenov. Review of snapshot spectral imaging technologies. *Optical Engineering*, 52(9):090901, 2013.

[10] N. Hagen, R. T. Kester, L. Gao, and T. S. Tkaczyk. Snapshot advantage: a review of the light collection improvement for parallel high-dimensional measurement systems. *Optical Engineering*, 51(11):111702, 2012.

[11] T. Okamoto and I. Yamaguchi. Simultaneous acquisition of spectral image information. *Optics letters*, 16(16):1277–1279, 1991.

[12] M. E. Gehm, R. John, D. J. Brady, R. M. Willett, and T. J. Schulz. Single-shot compressive spectral imaging with a dual-disperser architecture. *Optics Express*, 15(21):14013–14027, 2007.

[13] Y. Murakami, M. Yamaguchi, and N. Ohyama. Hybrid-resolution multispectral imaging using color filter array. *Optics Express*, 20(7):7173–7183, 2012.

[14] T. C. George, D. A. Basiji, B. E. Hall, D. H. Lynch, W. E. Ortyn, D. J. Perry, M. J. Seo, C. A. Zimmerman, and P. J. Morrissey. Distinguishing modes of cell death using the ImageStream® multispectral imaging flow cytometer. *Cytometry Part A*, 59(2):237–245, 2004.

[15] P. R. Griffiths and J. A. de Haseth. *Fourier transform infrared spectrometry.* John Wiley & Sons, 2nd edition, 2007.

[16] V. Saptari. *Fourier transform spectroscopy instrumentation engineering.* SPIE, 2004.

[17] A. Hirai, T. Inoue, K. Itoh, and Y. Ichioka. Application of multiple-image fourier transform spectral imaging to measurements of fast phenomena. *Optical Review*, 1(2):205–207, 1994.

[18] M. W. Kudenov and E. L. Dereniak. Compact snapshot real-time imaging spectrometer. *Proc. SPIE*, 8186:81860W, 2011.

[19] M. W. Kudenov and E. L. Dereniak. Compact real-time birefringent imaging spectrometer. *Optics Express*, 20(16):17973–17986, 2012.

[20] C. C. Montarou and T. K. Gaylord. Analysis and design of modified Wollaston prisms. *Applied Optics*, 38(31):6604–6616, 1999.

[21] Q. T. Liang. Simple ray tracing formulas for uniaxial optical crystals. *Applied Optics*, 29(7):1008–1010, 1990.

[22] E. Cojocaru. Direction cosines and vectorial relations for extraordinary-wave propagation in uniaxial media. *Applied Optics*, 36(1):302–306, 1997.

[23] M. Françon and S. Mallick. *Polarization Interferometers.* Applications in Microscopy and Macroscopy. Wiley, 1971.

[24] E. Hecht. *Optics.* Addison-Wesley, 4th edition, 2002.

[25] M. G. Nomarski. Microinterféromètre différentiel à ondes polarisées. *Journal de Physique et le Radium*, 16:9–13, 1955.

[26] M. G. Nomarski and A. R. Weill. Application à la métallographie des méthodes interférentielles à deux ondes polarisées. *Rev. Metall*, 2:121–128, 1955.

[27] R. J. Bell. *Introductory Fourier transform spectroscopy.* Academic Press, 1972.

[28] D. C. Cronemeyer. Electrical and optical properties of rutile single crystals. *Phys. Rev.*, 87:876–886, 1952.

[29] Edward D Palik. *Handbook of optical constants of solids*, volume 3. Academic press, 1998.

[30] E. R. Dobrovinskaya, L. A. Lytvynov, and V. Pishchik. *Sapphire: material, manufacturing, applications.* Springer, 2009.

[31] H. Luo, T. Tkaczyk, R. Sampson, and E. L. Dereniak. Birefringence of yttrium vanadate single crystals in the middle wavelength infrared. *Proc. SPIE*, 6119:61190J, 2006.

[32] Edmund Optics. Mid-Wave Infrared (MWIR) and Long-Wave Infrared (LWIR) Waveplates. `http://www.edmundoptics.com/optics/polarizers/waveplates-retarders/mid-wave-infrared-mwir-long-wave-infrared-lwir-waveplates/3401/`. Accessed: 2015-05-11.

[33] Thorlabs. MIR Wire Grid Polarizers on Silicon Substrates. `http://www.thorlabs.de/newgrouppage9.cfm?objectgroup_id=7515`. Accessed: 2015-05-11.

[34] J. W. Cooley and J. W. Tukey. An algorithm for the machine calculation of complex fourier series. *Mathematics of computation*, 19(90):297–301, 1965.

[35] Ontar Corporation. Hitran-PC 4.2. `http://www.ontar.com/software/productdetails.aspx?item=hitranpc`. Accessed: 2015-05-17.

[36] M. W. Kudenov, M. N. Miskiewicz, M. J. Escuti, and J. F. Coward. Polarization spatial heterodyne interferometer: model and calibration. *Optical Engineering*, 53(4):044104, 2014.